SARS-CoV-2 hijacks p38ß/MAPK11 to promote viral protein translation

Christina A. Higgins[1, 2, 3], Benjamin E. Nilsson-Payant[1, 3], Andrew P. Kurland[1, 2], Prithy Adhikary[1, 2], Ilona Golynker[1, 3], Oded Danziger[1, 3], Maryline Panis[1, 3], Brad R. Rosenberg[1, 3], Benjamin tenOever[1, 2, 3], and Jeffrey R. Johnson[1, 2, 4, 5]

[1]Department of Microbiology, Icahn School of Medicine at Mount Sinai, New York, NY, USA

[2]Global Health and Emerging Pathogens Institute, Icahn School of Medicine at Mount Sinai, New York, NY, USA

[3]Virus Engineering Center for Therapeutics and Research, Icahn School of Medicine at Mount Sinai, New York, NY, USA

[4]Corresponding author (jeffrey.johnson@mssm.edu)

[5]Lead contact

Further information and requests for resources and reagents should be directed to and will be fulfilled by the lead contact, Jeffrey R. Johnson (jeffrey.johnson@mssm.edu).

Summary

SARS-CoV-2, the causative agent of the COVID-19 pandemic, drastically modifies the cells that it infects. One such effect is the activation of the host p38 mitogen-activated protein kinase (MAPK) pathway, which plays a major role in inflammation pathways that are dysregulated in severe COVID-19 cases. Inhibition of p38/MAPK activity in SARS-CoV-2-infected cells reduces both cytokine production and viral replication. Here, we applied a systems biology approach to better understand interactions between the p38/MAPK pathway and SARS-CoV-2 in human lung epithelial cells. We found several components of the p38/MAPK pathway positively and negatively impact SARS-CoV-2 infection and that p38ß is a required host factor for SARS-CoV-2 that acts by promoting viral protein translation in a manner that prevents innate immune sensing. Furthermore, we combined chemical and genetic perturbations of p38ß with quantitative phosphoproteomics to identify novel, putative p38ß substrates in an unbiased manner, with broad relevance beyond SARS-CoV-2 biology.

Keywords

SARS-CoV-2, coronavirus, COVID-19, p38, MAPK, proteomics, phosphoproteomics

Introduction

Severe acute respiratory syndrome coronavirus 2 (SARS-CoV-2), the causative agent of the coronavirus disease 2019 (COVID-19) pandemic, has caused millions of deaths worldwide since it emerged in late 2019. While vaccines are highly effective at preventing severe illness and death, novel SARS-CoV-2 variants are continuously emerging with increased transmissibility and pathogenicity and it is possible that vaccines may be less effective against variants that arise in the future. Currently, only two drug therapies have proven efficacious for COVID-19 treatment: remdesivir, a nucleoside analog that targets the viral polymerase and provides a modest reduction in recovery time compared to placebo (Grein et al., 2020), and dexamethasone, a synthetic glucocorticoid with potent anti-inflammatory properties that reduced COVID-19 deaths by a third in ventilated patients and by a fifth for patients receiving supplemental oxygen (Grein et al., 2020; Group et al., 2020). An anti-inflammatory monoclonal antibody treatment targeting the IL-6 receptor, tocilizumab, has been the subject

of two clinical trials for COVID-19 treatment, but was not found to improve survival in either (Rosas et al., 2021; Salama et al., 2021). It is therefore imperative to continue to identify targets for COVID-19 therapeutic development to improve outcomes for severe COVID-19 cases.

Severe COVID-19 cases are associated with excessive inflammation in the lung that can lead to acute respiratory distress syndrome, respiratory failure, multi-organ failure, and death (Mehta et al., 2020; Merad and Martin, 2020). We previously reported in a phosphoproteomics study of SARS-CoV-2 infection that the p38 mitogen-activated protein kinase (MAPK) pathway becomes activated during infection and that inhibition of p38 reduces both inflammatory cytokine expression and SARS-CoV-2 replication, suggesting that p38 inhibition may target multiple mechanisms related to SARS-CoV-2 pathogenesis (Bouhaddou et al., 2020). While the mechanisms by which the p38/MAPK pathway regulates inflammatory cytokine gene expression and RNA stability are well described, the mechanism by which p38/MAPK inhibition reduces SARS-CoV-2 replication is unknown. Furthermore, the p38/MAPK pathway is comprised of four p38 kinase isoforms (p38α, p3β, p38γ, and p38δ) and at least six downstream effector kinases (MAPKAPK2, MAPKAPK3, MAPKAPK5, MSK1, MSK2, and MKNK1), but it is not known which kinases at which levels of the p38/MAPK pathway impact SARS-CoV-2 replication (Roux and Blenis, 2004).

Here we combined siRNA screening, chemical and genetic perturbations, and quantitative proteomics to better understand interactions between the p38/MAPK pathway and SARS-CoV-2 in infected cells. We identified p38ß as an essential host factor for SARS-CoV-2 replication and found that p38 inhibition reduced viral protein levels but did not impact viral mRNA levels. We applied an unbiased hierarchical clustering approach to identify putative p38ß substrates in the context of SARS-CoV-2 infection. Finally, we found that p38 inhibition reduced phosphorylation levels at multiple sites on the SARS-CoV-2 N protein.

Results

Meta-analysis of SARS-CoV-2 proteomics studies reveals pathways consistently regulated across species and cell types

To better understand the host response to SARS-CoV-2 infection, we performed a quantitative, unbiased analysis of changes in protein and phosphorylation site abundance by mass spectrometry-based proteomics (Figure 1A). Monoclonal A549 human lung epithelial cells expressing the SARS-CoV-2 ACE2 receptor (A549-ACE2) were infected with SARS-CoV-2 at a multiplicity of infection (MOI) of 0.1 in biological triplicate. At 24 hours post-infection, cells were lysed, digested with trypsin, and an aliquot subjected to Fe^{3+} immobilized metal affinity chromatography (Fe^{3+}-IMAC) to enrich for phosphorylated peptides. Samples were analyzed using a data-independent acquisition mass spectrometry (DIA-MS) approach for individual samples, and a data-dependent acquisition (DDA-MS) method to build a spectral library. Raw data were analyzed in Spectronaut to identify peptides, localize phosphorylation sites, build a spectral library from DDA-MS data, and extract intensity information from DIA-MS data (Bruderer et al., 2017). The data were subsequently analyzed by MSstats to build a model of variability, estimate fold-changes, perform significance testing, and adjust p-values for multiple testing (Choi et al., 2014).

In total, this analysis comprised 6,089 unique proteins groups and 16,032 unique phosphorylation site groups, with an average of approximately 5,000 protein groups and approximately 12,000 phosphorylation site groups per sample (Figure 1B). Throughout this study, we considered protein groups/phosphorylation site groups with $|\log_2\text{fold-change}| > 1$ and p-value < 0.05 to be differentially abundant. At the protein level, SARS-CoV-2 proteins (N, ORF1AB/NSP1, ORF1AB/NSP3, ORF9B, and S) were differentially increased by these criteria, and a limited number of host protein groups were differentially increased or decreased, consistent with SARS-CoV-2 suppression of host protein synthesis (Banerjee et al., 2002). We observed more changes in the phosphoproteome, with 98 and 33 phosphorylation site groups differentially increased and decreased, respectively (Figure 1C, Table S1).

We next compared these data with three published proteomics studies of SARS-CoV-2 infection (Bojkova et al., 2020; Bouhaddou et al., 2020; Stukalov et al., 2021). Pairwise Pearson correlation analysis of $\log_2$fold-change profiles for both protein abundance (Figure S1A) and phosphorylation (Figure 1D) data clustered primarily according to the species in which the data were collected. The data from Bouhaddou et al., which was collected in Vero E6 cells of African green monkey origin, were distinctly separated from our data and data from Stukalov et al. and Bojkova et al., which were collected in A549 and Caco-2 cells, respectively, and are both of human origin. We next performed a kinase activity analysis based on $\log_2$fold-change profiles using a gene set

enrichment analysis (GSEA) approach with kinase-substrate annotations derived from the PhosphoSite Plus resource (Beltrao et al., 2012; Hornbeck et al., 2015; Subramanian et al., 2005). Kinase activity profiles for data collected in human cell lines were strongly correlated, while profiles derived from A549 cells were somewhat anticorrelated with data collected in Vero E6 cells, and there was a modest correlation between data collected in Caco-2 and Vero E6 cells (Figure S1B, Table S2). This analysis identified GSK3B, ATR, p38α, MAPKAPK2, ABL, AMPKA1, mTOR, ATM, PLK1, and AURKB as the ten most commonly regulated kinases among all characterized kinases across the data sets examined (Figure 1E and Figure S1E). Kinases involved in cell cycle arrest - ATM, PLK1, and AURKB - were consistently regulated across all data sets, consistent with findings that SARS-CoV-2 infection leads to cell cycle arrest (Bouhaddou et al., 2020). Of particular interest to this study, the MAP kinase p38α and its downstream kinase, MAPKAPK2/MK2, were significantly regulated in all human studies and in several time points of the Vero E6 study. Inspection of the log_2fold-change profiles of individual substrates that contributed to each kinases' enrichment signals (the "leading edge" subset) revealed substrates that are commonly and differentially regulated across data sets (Figure 1F, Figure S1C, and Table S1). For p38α substrates, HSPB1/Hsp27 and BAZ1B were observed with increased phosphorylation in every data set collected thus far, while increased phosphorylation of other p38α substrates such as EGFR, ATF2, and MK2 was only detected in studies in human cell lines (Figure 1F; Table S4). Gene ontology enrichment analysis of log_2fold-change profiles of protein and phosphorylation group changes from all studies revealed similarities between Vero E6 and Caco-2 cells for downregulation of proteins in extracellular localizations. Caco-2 cells uniquely increased proteins in type I interferon signaling pathway ontology terms (Figure S1E, Table S3).

Multiple components of the p38/MAPK pathway impact SARS-CoV-2 infection in human lung epithelial cells

There remains a gap in understanding what components of the p38/MAPK pathway impact SARS-CoV-2 infection. Particularly understudied are functional differences between the four isoforms of p38: p38α/MAPK14, p38ß/MAPK11, p38γ/MAPK12, and p38δ/MAPK13. p38/MAPK also has several effector kinases immediately downstream of p38, including MAPKAPK2/MK2, MAPKAPK/MK3, MAPKAPK5/MK5, MSK1, MSK2, and MKNK1 (Figure 2A) (Roux and Blenis, 2004). To address this, we employed an siRNA screening methodology to assess how knockdown of p38 isoforms and their upstream and downstream regulators affect SARS-CoV-2 infection.

A549-ACE2 cells were transfected with siRNA pools targeting genes of interest, infected with SARS-CoV-2 for 36 hours, stained for SARS-CoV-2 nucleocapsid protein (N), and the percent cells infected was determined by immunofluorescence imaging cytometry. We identified p38ß as an essential host factor for SARS-CoV-2 infection, with approximately 90% reduction in infected cells and three log-fold reduction in virus titers when p38ß was knocked down compared to a non-targeting control (Figure 2B-C). Surprisingly, knockdown of p38α did not affect the percent of N-positive cells even though p38α and p38ß are often presumed to be functionally redundant. We also found that p38δ knockdown reduced infection by approximately 40% and that p38γ knockdown increased infection by approximately 50% (Figure 2B-C). Based on RNAseq analysis, p38α was expressed the highest in A549-ACE2 cells followed by p38γ, p38ß, and p38δ (Figure S2A). Of the downstream effector kinases, we found that only MSK2 knockdown reduced viral infection by approximately 65% (Figure 2B-C). We confirmed efficient siRNA knockdown of p38α, p38ß, p38γ, and MSK2 protein expression by western blotting (Figure 2D). We also verified that siRNA transfections did not affect cell viability for each of the siRNA pools (Figure S2B). Focusing next on upstream regulation of the p38/MAPK pathway, we again used siRNA screening to assess the effects of individual MAPKKK and MAPKK knockdown on viral infection. Among the MAPKKKs screened, we found that MAP3K8/TPL2/COT, MAP3K9/MLK1, and MAP3K11/MLK3 knockdown reduced SARS-CoV-2 infection by approximately 70%, 95%, and 80%, respectively, while MAP3K17/TAOK2/PSK knockdown increased infection by nearly 100% (Figure 2E). Cell viability was again not affected by siRNA transfection (Figure S2A). Finally, we confirmed by plaque assays significant reductions in virus titer upon MAP3K8, MAP3K9, and MAP3K11 knockdown (Figure 2F).

p38ß proviral mechanism is primarily STAT1-independent but leads to ISG expression as a byproduct

Given that the p38/MAPK pathway is known to regulate the gene expression and mRNA stability of many genes, we hypothesized that the proviral MAPK/p38 pathway kinases, p38ß, p38δ, and MSK2 may promote the expression of a host factor required for SARS-CoV-2 replication. We therefore assessed how siRNA knockdown of p38ß, p38δ, or MSK2 in the context of SARS-CoV-2 infection affects the host proteome during infection using quantitative proteomics. In biological quadruplicate, A549-ACE2 cells were transfected with siRNA pools targeting non-targeting control, p38ß, p38δ, or MSK2. Cells were then infected with SARS-CoV-2 at an MOI of

0.1, or mock-infected. At 36 hours post-infection, cells were lysed and subjected to trypsin digestion, Fe^{3+}-IMAC phosphopeptide enrichment, and DIA-MS analysis as described previously (Figure 3A). A total of 4,900 unique protein groups and 14,414 unique phosphorylation site groups were identified in these experiments (Figure 3B). These data clustered by their respective siRNA targets in both principal component and Pearson correlation analysis and each sample has similar log_2intensities (Figure S3A-F). In comparison to non-targeting control/mock-infected cells, non-targeting control/SARS-CoV-2-infected cells yielded few changes to the proteome and large changes to the phosphoproteome with approximately 1,000 phosphorylation site groups significantly increasing and decreasing. Knockdown of each kinase in SARS-CoV-2-infected cells led to more substantial changes to the proteome. Compared to non-targeting control/SARS-CoV-2-infected cells, knockdown of p38ß, p38δ, or MSK2, led to 287, 141, and 355 unique protein groups significantly increasing, respectively, and 274, 201, and 122 protein groups significantly decreasing compared to non-targeting control/mock-infected cells, respectively. There were also significant changes to the phosphoproteome in response to each of the kinase knockdowns, in comparison to non-targeting control/infected. Knockdown of p38ß, p38δ, or MSK2, led to 75, 842, and 474 unique phosphorylation site groups significantly increasing, respectively, and 339, 768, and 624 phosphorylation site groups significantly decreasing, respectively (Figure 3C, Table S1). Gene ontology enrichment analysis of protein abundance log_2fold-change profiles revealed that SARS-CoV-2 infected cells with siRNA-suppressed levels of p38ß or p38δ exhibited a strong type I interferon signature compared to infected cells transfected with a non-targeting control. In contrast, MSK2 knockdown in SARS-CoV-2-infected cells did not lead to a comparable type I interferon signature, further suggesting MSK2 is primarily not responsible for the p38ß phenotype (Figure 3D, Table S5). Looking specifically at well-characterized, anti-viral interferon-stimulated genes (ISGs), most were more upregulated in response to p38ß or p38δ knockdown in SARS-CoV-2-infected cells compared to non-targeting control SARS-CoV-2 infected cells (Figure 3E) (Schoggins and Rice, 2011). Western blotting confirmed that p38ß knockdown in SARS-CoV-2-infected cells led to an increase in MX1, a prototypical ISG (Figure S3G).

These findings led us to question whether p38ß knockdown reduced SARS-CoV-2 replication by leading to the expression of ISGs that restrict viral replication, or if p38ß knockdown reduced viral replication in a primarily ISG-independent manner that incidentally led to the expression of ISGs, for example, by exposing a pathogen-associated molecular pattern (PAMP) that is sensed by the innate immune system. To address this, we

compared SARS-CoV-2 infection and p38ß, p38δ, or MSK2 siRNA knockdown in A549-ACE2 cells to STAT1-knockout A549-ACE2 cells which are unable to activate STAT1-dependent ISG expression. If STAT1-dependent expression of ISGs is required to restrict infection in cells with reduced p38ß/δ expression, deletion of STAT1 will restore SARS-CoV-2 replication to wild-type levels. We found that the reduction in SARS-CoV-2 infection in p38ß, p38δ, or MSK2 siRNA-transfected cells is not appreciably rescued by STAT1-knockout, indicating that the mechanisms of action of these p38/MAPK pathway kinases are primarily ISG- and STAT1-independent (Figure 3F-G). We confirmed by Western blotting STAT1 knockout and ablation of MX1 expression as well as STAT1 phosphorylation in the A549ΔSTAT1-ACE2 cells, and efficient knockdown of the kinases of interest by siRNA transfection (Figure 3G). These findings demonstrate that the interferon signature caused by p38ß and p38δ knockdown is not the primary mechanism by which p38 inhibition reduces SARS-CoV-2 infection.

Quantitative phosphoproteomics identifies novel p38ß substrates in an unbiased manner

We next sought to better understand how the host phosphoproteome of SARS-CoV-2-infected cells changes in response to p38 inhibition to identify putative p38ß substrates that may explain the mechanism by which it reduces SARS-CoV-2 infection. We employed three strategies to identify p38ß substrates: (1) siRNA knockdown of p38ß (described above); (2) titration of a p38α/ß inhibitor, SB203580, for 1 hour preceding SARS-CoV-2 infection for 24 hours (pre-treatment), and (3) infection with SARS-CoV-2 for 24 hours with the last 4 hours of infection in the presence of SB203580 treatment (terminal treatment). We selected the p38 inhibitor SB203580 as it is well-characterized and specific for p38α/ß (Cuenda et al., 1995). In all cases, cells were lysed and subjected to proteome and phosphoproteome analysis as described previously (Figure 4A). These data clustered by their respective conditions in both principal component and Pearson correlation analysis and each sample has similar $\log_2$intensities within each experiment (Figure S4A-F and S4I-N). The terminal drug treatment experiment yielded 16,220 unique phosphorylation site groups and 16,032 unique phosphorylation site groups were identified with the pre-treatment experiment (Figure 4B). Comparing SARS-CoV-2 infected, DMSO terminal treatment to mock-infected, DMSO terminal treatment conditions yielded 875 differentially increased and 294 differentially decreased phosphorylation site groups. More subtle changes were observed comparing SARS-CoV-2 infected, SB203580 terminally treated compared to SARS-CoV-2 infected, DMSO terminally treated

conditions, with only 23 and 145 phosphopeptide groups significantly increased and decreased, respectively. As for the pre-treatment observations, 98, 54, and 30 phosphopeptide groups differentially increased and 33, 123, and 68 phosphopeptide groups differentially decreased, in SARS-CoV-2 infected/DMSO treated fold over mock-infected/DMSO-treated, infected/1μM SB203580-treated fold over infected/DMSO-treated, and infected/10μM SB203580-treated fold over infected/DMSO-treated, respectively (Figure 1C, Table S1). We observed a significant decrease in phosphorylation of known p38 substrates, CP131 at S47, HSPB1 at S15, PARN at S557, RIPK1 at S320, in response to SB203580 in both pre-treatment and terminal treatment experiments, which confirmed effectiveness of the drug treatment with both approaches (Figure S4G and S4O). We combined these phosphoproteome profiles with p38ß knockdown profiles and developed an unbiased hierarchical clustering approach to identify novel, putative p38ß substrates. First, $\log_2$fold-change profiles were hierarchically clustered based on their Euclidian distances (Figure 4D). Any profiles with missing values in any condition were excluded from this analysis. The data subjected to hierarchical clustering contained 1,191 phosphorylation profiles in total and 12 phosphorylation profiles annotated in Phosphosite Plus to be substrates of p38α, p38ß, or one of their downstream effector kinases (i.e., MK2, MK3, MK5, MSK1, MSK2, or MKNK1) (Hornbeck et al., 2015). The data were then clustered into 2 to 100 clusters by cutting the dendrogram tree in order of decreasing height, and for each iteration the significance of enrichment of p38α/ß substrates in each cluster was calculated by a hypergeometric test. The best enrichment of p38α/ß substrates was achieved when the data were separated into 3-12 clusters (Figure 4E). The cluster most significantly enriched for p38α/ß substrates occurred in iterations 3-12 and contained 35 phosphorylation sites in total with 3 annotated p38α/ß substrates (HSPB1, RBM7, and TIF1B; hypergeometric p-value = 0.005) (Figure 4F, Table S6). This group of novel, putative p38ß substrates includes several annotated p38α/ß substrates at phosphorylation positions not annotated as p38α/ß-dependent (TIF1B, HSPB1, NELFE), and proteins physically associated with annotated p38α/ß substrates (LARP7, TIF1A) (Figure 4G). This cluster is enriched for processes commonly associated with the p38/MAPK pathway, including RNA binding, protein folding, and transcription elongation (Figure 4G and S4H) (Roux and Blenis, 2004).

p38ß promotes viral protein translation in human lung epithelial cells

In addition to identifying novel host p38 substrates, we also explored possible p38-dependent phosphorylation of SARS-CoV-2 proteins. In order to focus on viral phosphorylation sites, we specifically looked at the short, terminal drug treatment dataset because the short drug treatment is effective at inhibiting p38α/ß kinases but does not affect total viral protein abundance. This allowed us to accurately quantify changes to viral phosphorylation sites in response to p38 inhibition independent of viral protein abundance. In our analyses, SARS-CoV-2 N was the only viral protein identified with significantly changing p38-dependent phosphorylation sites based on p-values, although the fold-changes were less than the 2-fold threshold we implemented throughout this study. Four identified phosphosites (S21, S23, T24, and S26) significantly decreased during infection in response to SB203580 compared to DMSO treatment (Figure 5A and S5A). These sites are located in a poorly characterized, disordered region close to the N-terminus of N, adjacent to the N-terminal RNA-binding domain (NTD). Additionally, these amino acid residues have no or relatively low entropy amongst SARS-CoV-2 variants in the Nextstrain resource, indicating they are well conserved among variants of SARS-CoV-2 (Figure 5A) (Hadfield et al., 2018). We confirmed no significant difference in total N expression between DMSO-treated/infected and SB203580-treated/infected cells (Figure 5B).

To further elucidate the mechanism of action responsible for the proviral behavior of p38ß, we performed a high MOI, single cycle infection with SARS-CoV-2 in A549-ACE2 cells transfected with non-targeting or p38ß siRNA, and analyzed host and viral mRNA using next-generation sequencing. We compared SARS-CoV-2 genomic RNA coverage by considering the number of viral reads at each nucleotide position and observed that there was no significant difference in genome coverage comparing cells infected and treated with siRNA targeting p38ß compared to control, suggesting p38ß does not play a role in regulating genomic RNA replication versus subgenomic RNA transcription (Figure 5C). Surprisingly, percentage viral reads did not change between cells infected and transfected with non-targeting control siRNA compared to p38ß siRNA, even though p38ß protein expression was significantly reduced (Figure 5D), and previous data showed drastic decrease in viral replication during multicycle infections with p38ß knockdown (Figure 2B-C, Table S7). GO term enrichment analysis of differential gene expression data from p38ß siRNA transfected over non-targeting control siRNA transfected infected cells supports previous findings including the upregulation of type I interferon signaling (Figure 5E, Table S8). GO term enrichment analysis of SARS-CoV-2 infected, control transfected fold over mock-infected, control transfected gene expression data revealed upregulation of MAPK signaling pathway regulation

and extracellular matrix organization, supporting previous findings (Figure S5C, Table S9). To further assess SARS-CoV-2 replication in a single-cycle setting, viral subgenomic mRNA, genomic mRNA, and protein levels were measured after a high MOI, single-cycle infection with SARS-CoV-2 in A549-ACE2 cells transfected with siRNA targeting p38/MAPK members. Again, there was no significant difference in genomic RNA abundance (i.e. nsp14) compared to subgenomic mRNA abundance (i.e. trs-N and trs-S) with p38ß inhibition compared to non-targeting control. Also, normalized to SARS-CoV-2 infected cells transfected with non-targeting control siRNA, knockdown of SARS-CoV-2 N resulted in similar decreases in N-positive cells and viral transcript expression, but knockdown of p38ß resulted in significant decrease in N-positive cells, but no significant change in viral transcript abundance (Figure 5F). These findings suggest the proviral activity of p38ß promotes viral protein translation.

Discussion

In this study, we systematically characterized the p38/MAPK pathway in the context of SARS-CoV-2 infection using a combination of genetics, genomics, and proteomics approaches. We identified the specific segments of the p38/MAPK pathway that impact SARS-CoV-2 infection and discovered p38/MAPK substrates in an unbiased manner. We found that p38ß is the major component of the p38/MAPK pathway contributing to SARS-CoV-2 infection and that it does so at the stage of viral protein translation. These findings inform on basic SARS-CoV-2 biology, identify novel drug targets for the treatment of COVID-19, and provide a methodological approach for the identification of kinase substrates that can be broadly applied to many areas of research.

The p38/MAPK pathway activity is significantly increased during SARS-CoV-2 infection in human lung epithelial cells

There are many documented mechanisms by which the p38/MAPK pathway becomes activated in the context of viral infections. The PDZ-binding motif of SARS-CoV envelope protein and SARS-CoV 7a protein have been shown to potently activate the p38 pathway, but it is not known whether these activities are conserved for SARS-CoV-2 (Jimenez-Guardeno et al., 2014; Kopecky-Bromberg et al., 2006). *In vivo*, SARS-CoV-2 infection leads to the production of an inflammatory cytokine signature that includes IL-6 and TNFα, which are well documented

to activate the p38/MAPK pathway (Karki et al., 2021). In the present study, we show that knockdown of MAP3K8, MAP3K9, or MAP3K11 significantly inhibited SARS-CoV-2 infection in a manner similar to p38 inhibition. This was surprising as MAPKKKs are generally thought to be more functionally redundant, but these data suggest that specific MAPKKKs contribute to p38/MAPK pathway signal transduction in the context of SARS-CoV-2 infection. Given that MAPKKKs are typically activated by G-protein coupled receptors associated with receptors on the cell surface, such as cytokine receptors, we favor a model whereby the p38/MAPK pathway becomes activated as a result of cytokine production, but alternative mechanisms are plausible.

p38ß is required for SARS-CoV-2 replication in human lung epithelial cells

Pyridinyl imidazole class inhibitors (i.e. SB203580, etc.), act by reversibly binding the ATP pocket of the enzyme and preventing enzymatic activity, primarily inhibiting p38α and p38ß as they have larger pockets than p38γ and p38δ (Han et al., 2020). They were widely used to characterize the p38 kinases prior to the advent of genetic perturbation approaches like RNAi and CRISPR. As p38α and p38ß have 75% sequence similarity between them, these two isoforms have been generally presumed to be functionally redundant. However, pyridinyl imidazole class inhibitors are ten-fold more effective at inhibiting p38α than p38ß. Many phosphorylation sites annotated as p38ß substrates were identified using these inhibitors and thus would benefit from further inspection with modern genetic or chemical biology approaches such as analog-sensitive kinase inhibition. Additionally, there are documented functional differences between p38α and p38ß. p38α knockout mice are embryonically lethal whereas p38ß knockout mice are viable and fertile (Beardmore et al., 2005). p38ß has also been shown to be uniquely capable of auto-phosphorylation (Beenstock et al., 2016). In the present study, we show p38ß, but not p38α, is required for SARS-CoV-2 replication in human lung epithelial cells. These data, in addition to other p38ß-focused research, emphasize the need for p38ß-specific inhibitors and reagents to help better characterize this isoform. p38ß does not appear to be essential and it has a distinctly smaller active site than p38α that may allow for the development of specific inhibitors, thus we believe p38ß may make an attractive target. Additional studies are needed to determine if p38ß is important for the replication of other coronaviruses and other virus families.

Identification of novel p38ß substrates

We globally quantified changes to the phosphoproteome in response to several perturbations affecting p38/MAPK signal transduction including a pretreatment with two concentrations of p38 inhibitor before SARS-CoV-2 infection, a short treatment with p38 inhibitor in the last 4 hours of SARS-CoV-2 infection, and p38 isoform knockdown by siRNA before SARS-CoV-2 infection. In combination, these data allowed us to extract log_2fold-change profiles of annotated p38 substrate phosphorylation sites in response to these perturbations and to identify novel, putative p38ß substrates based on the similarity of their profiles to annotated p38 substrate profiles. We developed a hierarchical clustering approach and an unbiased method to determine the optimal number of clusters. This approach is broadly applicable for kinases for which some annotated substrates have been identified and for which specific inhibitors are available. It could be advantageous to perturb the system with multiple inhibitors, inhibitor concentrations, or time points to separate off- and on-target inhibitor effects and to develop more specific substrate profiles to feed into the clustering algorithm. One limitation of this approach is that it cannot determine whether the substrates identified were direct substrates of the kinase of interest.

SARS-CoV-2 N contains p38-dependent phosphosites

Throughout the viral life cycle, coronavirus nucleocapsid protein (N) performs many crucial functions including oligomerizing along the length of viral RNA for protection, enhancing viral polymerase activity, modulating template switching, and innate immunity evasion (Chang et al., 2014). Post-translational modifications on N have been documented to affect N activities. Phosphorylation of avian *Gammacoronavirus* infectious bronchitis virus N has been shown to increase the affinity of N for viral RNA compared to non-viral RNA (Chen et al., 2005). Additionally, phosphorylation of *Betacoronavirus* murine hepatitis virus (MHV) N by GSK-3 has been shown to regulate replication of genomic RNA versus subgenomic RNA by promoting template read-through (Wu et al., 2014). In this study, we identified phosphosites on SARS-CoV-2 N that were p38-dependent, although their fold-changes were more modest compared to that of host p38 substrates that were quantified. As N phosphorylation is known to affect its activity, it is plausible that p38-dependent N phosphorylation is responsible for the phenotypes we observed, but we cannot exclude the possibility that p38-dependent phosphorylation of a host

protein may drive these phenotypes. Further experiments are required to determine the impact of novel p38ß phosphorylation substrates on SARS-CoV-2 infection.

p38ß promotes translation of viral proteins

p38 pathway signal transduction promotes MHV protein translation by acting through p38α/ß-mediating kinase, MKNK1, in order to promote cap-dependent translation by phosphorylating eIF4E (Banerjee et al., 2002). Our data also suggest that p38ß activity promotes coronavirus protein translation, however, here we show knockdown of MKNK1 has no effect on SARS-CoV-2 protein expression (Figure 2B). Reduced mRNA cap guanine-N-7 methylation by NSP14 of *Alphacoronavirus* porcine epidemic diarrhea virus transcripts leads to inefficient replication and ISG induction (Lu et al., 2020). It is possible that p38ß activity promotes protein-protein interactions that support viral protein translation. Further inspection is needed to further characterize the mechanism of action exerted by p38ß to promote viral protein translation.

Methods

Cells

A549 cells, a human lung epithelial cell line (A549, ATCC®, CCL-185), HEK 293T cells, a human kidney epithelial cell line (HEK 293T/17, ATCC®, CRL-11268), and Vero E6 cells (Vero 76, clone E6, Vero E6, ATCC® CRL-1586), an African Green Monkey kidney epithelial cell line, were authenticated by ATCC. A monoclonal ACE2-expressing A549 cell line was a kind gift from Brad Rosenberg. Monoclonal ACE2-expressing STAT1-knockout A549 cells were generated as previously described (Aydillo et al., 2018; Daniloski et al., 2021; Seifert et al., 2019). All cell lines were cultured under humidified 5% CO_2 conditions in 10% v/v fetal bovine serum (FBS, Thermo Fisher Scientific) and 100 I.U. penicillin and 100 µg/mL streptomycin (Pen/Strept, Corning) in Dulbecco's Modified Eagle Medium (DMEM, Corning). Cells were confirmed negative for mycobacteria monthly (Lonza).

Viruses

SARS-CoV-2 strain USA/WA1/2020 was used for all SARS-CoV-2 infections. Virus stocks were grown on Vero E6 cells. Supernatant was collected 30h post-infection and concentrated through a 100 kDa centrifugal filter unit (Amicon). Concentrated virus was washed thrice in phosphate-buffer saline (PBS) and concentrated with a 100 kDa centrifugal filter unit. Virus titers were determined by plaque assay on Vero E6 cells.

Cell Lysis and Digestion

Cells were washed twice in PBS. Cells were lysed in urea lysis buffer containing 8 M urea, 100 mM ammonium bicarbonate (ABC), 150 mM NaCl, protease inhibitor and phosphatase inhibitor cocktail (Thermo Fisher Scientific). Lysates were probe sonicated on ice 3 × 1s at 50% power, with 5s of rest in between pulses. Protein content of the lysates was quantified using a micro BCA assay (Thermo Fisher Scientific). 1mg of protein per sample was treated with (Tris-(2-carboxyethyl)phosphine (TCEP) to a final concentration of 4 mM and incubated at room temperature (RT) for 30 minutes. Iodoacetamide (IAA) was added to each sample to a final concentration of 10 mM, and samples were incubated in the dark at RT for 30 minutes. IAA was quenched by dithiothreitol (DTT) to a concentration of 10 mM and incubated in the dark at RT for 30 minutes. Samples were then diluted with 5 sample volumes of 100 mM ABC. Trypsin Gold (Promega) was added at a 1:100 (enzyme:protein w/w) ratio and lysates were rotated for 16 hours at RT. 10% v/v trifluoroacetic acid (TFA) was added to each sample to a final concentration of 0.1% TFA. Samples were desalted under vacuum using Sep Pak tC18 cartridges (Waters). Each cartridge was first washed with 1 mL 80% acetonitrile (ACN)/0.1% TFA, then with 3 × 1 mL of 0.1% TFA in H_2O. Samples were then loaded onto cartridges. Cartridges were washed with 3 x 1 mL of 0.1% TFA in H_2O. Samples were then eluted with 1 mL 40% ACN/0.1% TFA. 20 µg of each sample was kept for protein abundance measurements, and the remainder was used for phosphopeptide enrichment. Samples were dried by vacuum centrifugation. Protein abundance samples were resuspended in 0.1% formic acid (FA) for mass spectrometry analysis.

Phosphopeptide enrichment

For each sample batch and under vacuum, 500µL (30µL per sample) of 50% Ni-NTA Superflow bead slurry (QIAGEN) was added to a 2 mL bio-spin column. Beads were washed with 3 × 1mL HPLC H_2O, incubated with

4 × 1mL 100 mM EDTA for 30s, washed with 3× 1mL HPLC H_2O, incubated 4 × 1mL with 15 mM $FeCl_3$ for 1 minute, washed 3 × 1mL HPLC H_2O, and washed once with 1mL of 0.5% v/v FA to remove residual iron. Beads were resuspended in 750 µL of 80% ACN/0.1% TFA. 1mg of digested peptides were resuspended in 83.33 µL 40% ACN/0.1% TFA and 166.67 µL 100% ACN/0.1% TFA and 60 µL of the bead slurry were added to each sample and incubated for 30 minutes while rotating at RT. A C18 BioSPN column (Nest Group), centrifuged at 110xg for 1 minute each step, was equilibrated with 2 × 200 µL 80% ACN/0.1% TFA. Beads were loaded onto the column and washed with 4 × 200 µL 80% ACN/0.1% TFA, then washed 3 × 200 µL 0.5% FA. Then, 2 × 200 µL 500 mM potassium phosphate buffer pH 7 was added to the column and incubated 1 minute. Then, 3 × 200 µL 0.5% FA were added to column. Phosphopeptides were eluted with 2 × 100 µL of 40% ACN/0.1% FA and vacuum centrifuged to dryness. Phosphopeptides were resuspended in 25 µL 4% FA/3% ACN for mass spectrometry analysis.

Mass spectrometry data acquisition

All samples were analyzed on an Orbitrap Eclipse mass spectrometry system (Thermo Fisher Scientific) equipped with an Easy nLC 1200 ultra-high pressure liquid chromatography system (Thermo Fisher Scientific) interfaced via a Nanospray Flex nanoelectrospray source. For all analyses, samples were injected on a C18 reverse phase column (30 cm x 75 µm (ID)) packed with ReprosilPur 1.9 µm particles). Mobile phase A consisted of 0.1% FA, and mobile phase B consisted of 0.1% FA/80% ACN. Peptides were separated by an organic gradient from 5% to 35% mobile phase B over 120 minutes followed by an increase to 100% B over 10 minutes at a flow rate of 300 nL/minute. Analytical columns were equilibrated with 6 µL of mobile phase A. To build a spectral library, samples from each set of biological replicates were pooled and acquired in data dependent manner. Protein abundance samples were fractioned with Field Assymetric Ion Mobility Spectrometry (FAIMS) fractionation with a FAIMS Pro device (Thermo Fisher Scientific). Each pooled sample was analyzed four times with four FAIMS compensation voltages (CV) (-40V,-55V,-65V,-75V). Data dependent analysis (DDA) was performed by acquiring a full scan over a m/z range of 375-1025 in the Orbitrap at 120,000 resolving power (@200 m/z) with a normalized AGC target of 100%, an RF lens setting of 30%, and an instrument controlled ion injection time.-Dynamic exclusion was set to 30 seconds, with a 10 ppm exclusion width setting. Peptides with charge states 2-6 were selected for MS/MS interrogation using higher energy collisional dissociation (HCD) with

a normalized HCD collision energy of 28%, with three seconds of MS/MS scans per cycle. Similar settings were used for data dependent analysis of phosphopeptide enriched pooled samples, with a Dynamic Exclusion of 45 seconds and no FAIMS fractionation. Data-independent analysis (DIA) was performed on all individual samples. An MS scan at 60,000 resolving power over a scan range of 390-1010 m/z, an instrument controlled AGC target, an RF lens setting of 30%, and an instrument controlled maximum injection time, followed by DIA scans using 8 m/z isolation windows over 400-1000 m/z at a normalized HCD collision energy of 28%.

Drug treatment following virus infection

2×10^7 ACE2-A549 cells in 15cm plate format were infected in quadruplicate, in duplicate, with SARS-CoV-2 at an MOI 0.1 in 25mL infection media. $2x10^7$ ACE2-A549 cells in 15cm plate format were mock-infected in quadruplicate in 25mL infection media. 20 hours post-infection, half of the infected replicates were treated with SB203580 in DMSO at a final concentration of 10μM and the other half of the infected replicates were treated with an equal volume of DMSO. 4 hours after drug treatment, cells were lysed in urea lysis buffer.

siRNA knockdown

2×10^4 ACE2-A549 cells in a 96-well plate format were transfected in triplicate, in triplicate, with 1pmol ON TARGETplus siRNA pools (Dharmacon) prepared in 10uL/replicate Opti-MEM (Corning) with a 1:3 ratio of siRNA:RNAiMax (Thermo Fisher Scientific). 48 hours post-transfection, cells were infected with SARS-CoV-2 at a MOI of 0.1 or 2 in infection media (2% FBS, Pen/Strept, in DMEM). 8-, 24-, 30-, or 36-hours post-infection, supernatants were saved for plaque assay, one-third of replicates were fixed in 5% paraformaldehyde (PFA) in PBS for 24 hours, one-third of replicates were lysed in RIPA buffer with SDS (50mM Tris HCl, 150mM sodium chlorate, 1% v/v Triton X-100, 0.5% v/v sodium deoxycholate, 1% w/v sodium dodecyl sulfate, and protease inhibitors (MilliporeSigma) and saved for immunoblotting, and then last third of replicates were lysed in RLT buffer (QIAGEN) and saved for RNA extraction and RT-qPCR analysis.

Immunofluorescence Assay

Cells were washed with PBS and permeabilized for 10 minutes in 0.2% v/v Triton X-100 in PBS. Cells were incubated in blocking buffer (3% w/v BSA, 0.1% v/v Triton X-100, 0.2% w/v fish gelatin in PBS) at room

temperature for one hour. Cells were incubated in primary antibody (1:1000 mouse anti-SARS N IC7 antibody, a kind gift from Thomas Moran) in antibody buffer (1% w/v BSA, 0.03% v/v Triton X-100, 0.1% fish gelatin in PBS) overnight at 4C. Cells were washed thrice in PBS. Cells were incubated in 1:1000 anti-mouse AlexaFluor488 or anti-mouse AlexaFluor594 (Thermo Fisher Scientific) and 4',6-diamidino-2-phenylindole counterstain (DAPI, Thermo Fisher Scientific) in antibody buffer at room temperature for one hour. Cells were washed thrice in PBS and imaged in 100uL PBS on a Celígo Imaging Cytometer (Nexcelcom Bioscience). Celígo software was used to quantify number of cells by DAPI nuclear staining and number of infected cells by N staining. Percentage of cells infected was calculated as follows: 100*((count of green-positive cells – count of green-positive cells without blue-positive count) / count of blue-positive cells) to account for total cell number, infected cell number, and exclude green-positive debris. Error bars indicate standard deviation of three technical replicates from a representative biological replicate. Two-tailed paired student's t-tests for unequal variance were performed to generate p-values. All experiments were performed in at least biological triplicate.

Plaque Assay

Virus-containing supernatant was serially 10-fold diluted in infection media. 100uL inoculum was added to confluent Vero E6 cells in a 24-well plate format and incubated at room temperature one hour and agitated often to avoid drying. 1mL semi-solid overlay (0.1% w/v agarose, 4% v/v FBS, and Pen/Strept in DMEM) was added to each well and plate were incubated at 37C for 48-72 hours until sizeable plaques formed. Cells were fixed in 5% PFA in PBS for 24 hours at room temperature. Cells were washed twice with water. Cells were incubated in 0.5mL staining dye (2% w/v crystal violet, 20% v/v ethanol in water) for 30 minutes at room temperature. Stained cells were washed with water and allowed to dry before plaques were counted and plaque-forming units per mL was calculated as follows: ((# of plaques)/(mL of inoculum*$10^{\text{dilution factor}}$)). Error bars indicate standard deviation of three technical replicates from a representative biological replicate. Two-tailed paired student's t-tests for unequal variances were performed to generate p-values. All experiments were performed in at least biological triplicate.

Western blotting

Lysates were incubated at 95C for 10 minutes in Laemmli sample buffer (Bio-Rad Laboratories). Lysates were run on an SDS-PAGE gel with a protein ladder standard (Bio-Rad Laboratories) and transferred to a nitrocellulose membrane (Bio-Rad Laboratories). Blots were incubated in 5% milk in TBST for one hour at room temperature. Blots were incubated in primary antibody in 1% milk in TBST overnight at 4C. Blots were washed thrice for 5 minutes in TBST. Blots were incubated in secondary HRP-conjugated or infrared-conjugated secondary antibody in 1% milk in TBST. Blots were washed thrice for 5 minutes in TBST. Blots were imaged on a Chemiluminescence digital imager (Bio-Rad Laboratories) using FEMTO ECL reagent (Thermo Fisher Scientific) or an infrared digital imager (LICOR Biosciences).

Cell viability assay

2×10^4 ACE2-A549 cells in a 96-well white-bottom plate were transfected in triplicate with siRNA pools. 72 hours post-transfection, plate was equilibrated to room temperature for 30 minutes. 100uL of Titerglo buffer with substrate was added to each well (Promega Corporation). Plate was nutated at room temperature for 2 minutes to lyse the cells. Plate was incubated at room temperature for 10 minutes. Plate was read for luminescence end-point kinetics with a 1s integration on a Cytation 5 Plate Reader using Gen5 software (Biotek Instruments). Relative luminescence units for each siRNA condition were normalized to non-targeting control siRNA and displayed as a percentage. Two-tailed paired student's t-tests for unequal variances were performed to generate p-values. Error bars indicate standard deviation of three technical replicates from a representative biological replicate. All experiments were performed in at least biological triplicate.

RNA extraction and RT-qPCR analysis

Cells were lysed in RLT buffer and RNA was extracted using a RNeasy 96 kit (QIAGEN) according to the manufacturer's protocol. 1-step RT-qPCR was performed on 2μL of RNA using the Luna® Universal One-Step RT-qPCR Kit (NEB Biosciences) and primers for ß-tubulin (F: 5'-GCCTGGACCACAAGTTTGAC-3'; R: 5'-TGAAATTCTGGGAGCATGAC-3'), SARS-CoV-2 nsp14 (F: 5'-TGGGGYTTTACRGGTAACCT-3'; R: 5'-AACRCGCTTAACAAAGCACTC-3') , TRS-N (F: 5'-CTCTTGTAGATCTTCTCTAAACGAAC-3'; R: 5'-GGTCCACCAAACGTAATGCG-3'), and TRS-Spike (F: 5'-CTCTTGTAGATCTTCTCTAAACGAAC-3'; R: 5'--3') as previously described (Daniloski, Jordan et al. 2020; Chu et al. 2020). Reactions were ran and analyzed on a

Lightcycler 480 II Instrument (Roche). ΔΔ cycle threshold values were calculated relative to mock-infected samples. Error bars indicate standard deviation of three biological replicates. Two-tailed paired student's t-tests for unequal variances were performed to generate p-values.

mRNA sequencing and analysis

2×10^5 ACE2-A549 cells were transfected with siRNA pools as previously indicated. 48 hours post-transfection, cells were infected with SARS-CoV-2 at an MOI of 0.75 in infection media. 8 hours post-infection, cells were lysed in 1mL of Trizol (Invitrogen). RNA was extracted and DNase I treated using Direct-zol RNA Miniprep kit (Zymo Research) according to the manufacturer's protocol. RNA-seq libraries of polyadenylated RNA were prepared with the TruSeq RNA Library Prep Kit v2 (Illumina) or TruSeq Stranded mRNA Library Prep Kit (Illumina) according to the manufacturer's protocols. Libraries were sequenced with a Illumina NextSeq 500 platform. Raw sequencing reads were aligned to the hg19 human genome with the Basespace RNA-Seq Aligment application (Illumina). GO-term enrichment was performed using Biojupies (Torre et al. 2018) and visualized using ggplot2 (Wickham 2016). Alignments to viral genomes was performed using bowtie2 (Langmead and Salzberg, 2012). The SARS-CoV-2 USA/WA1/2020 strain genome was used for analysis in this study (GenBank: MN985325). Genome coverage (viral gene counts at each nucleotide position) was analyzed using Integrative Genomics Viewer and visualized with ggplot2 (Robinson et al., 2011). Genome schematic was created with BioRender (BioRender.com).

Mass spectrometry data analysis

All raw mass spectrometry data generated in this study were analyzed by the Spectronaut software suite (Biognosys) (Bruderer et al., 2017). DDA-MS data were analyzed to build a spectral library by searching against a protein sequence database comprised of SwissProt human sequences (downloaded on October 10, 2019) and SARS-CoV-2 strain USA/WA1/2020 sequences using Biognosys factory settings, which considered a static modification for cysteine carbamidomethylation and variable modifications for methionine oxidation and protein N-terminal acetylation. We added variable modifications for serine/threonine/tyrosine phosphorylation for phosphoenriched samples. All DDA-MS runs generated in this study were combined to make one spectral

library against which all DIA-MS data were analyzed. DIA-MS data were also analyzed by Spectronaut to extract fragment ion intensity information based on the spectral library described above using Biognosys factory settings. The data were exported as a tab-delimited, MSstats-formatted report.

Spectronaut reports were analyzed by the MSstats package in the Rstudio statistical programming environment (Bruderer et al., 2017). Before MSstats analysis, protein group accessions were converted to phosphorylation site group accessions with a Perl script. Data were processed by MSstats to equalize medians, summarize features using Tukey's median polish, and impute missing values by accelerated failure model. Intensities below the 0.999 quantile were considered missing values. Principal component analysis was performed on MSstats estimated intensities using the prcomp function in R and the first two principal components plotted for all data sets. Sample correlation analysis was performed by pairwise Pearson correlation coefficient calculation in R.

Gene ontology (GO) enrichment and kinase activity analyses

GO enrichment and kinase activity analyses were performing using the GSEA method with the fgsea package in R (Subramanian et al., 2005). For kinase activity analysis, kinase substrate interactions were derived from the PhosphositePlus Kinase Substrate Dataset (Hornbeck et al., 2015). Protein substrates of each kinase were compiled into gene sets. For gene ontology enrichment analysis, GO terms and definition were downloaded from the gene ontology resource (downloaded on February 18, 2021) and genes within each GO term were grouped together as gene sets. For both Go enrichment analysis and kinase activity analysis, for each comparison considered, the data were ranked by $\log_2$fold-change subjected to fgsea testing using the gene sets described above.

Unbiased identification of p38β substrates

For hierarchical clustering, comparison indicated in Figure 4 were first filtered missing logfold-change values in any condition. Distances were calculated based on Euclidian distance using the dist function in R and the data were hierarchically ordered using the hclust function in R. Next, the data were divided into *n* clusters in decreased order of dendrogram height in 99 iterations with *n* ranging from 2 to 100 using the cutree function in R. For each iteration, the enrichment of annotated p38α/β substrates within each cluster was calculated using a hypergeometric test with the dhyper function in R. P-values were adjusted by Benjamini-Hochberg method with the p.adjust function in R (Benjamini and Hochberg, 1995). Annotations of p38α/β substrates were derived from the Phosphosite Plus Kinase Substrate data set (Hornbeck et al., 2015). Phosphorylation sites in the cluster with the minimum hypergeometric p-value in all iterations across all clusters comprises our putative p38β substrates.

Acknowledgments

We would like to acknowledge the following funding sources: NIH R01 AI151029, NIH U01 AI150748 (BRR), and NIH U19AI118610 (JRJ).

Author Contributions

Conceptualization: CAH, JRJ

Proteomics sample preparation: CAH, APK, PA

Proteomics data acquisition: APK

Cell line generation: OD

Experiments: CAH

RNA-seq preparation and acquisition: MP

RT-qPCR: IG

Data analysis: JRJ, CAH

Figure generation: JRJ, CAH

Manuscript Preparation: JRJ, CAH

Manuscript editing: BT, BRR, OD, BENP, CAH, JRJ

Literature Review: JRJ, CAH

Work Supervision: BRR, BT, JRJ

Declaration of Interests

The authors have no competing interests to declare.

Figure Legends

Figure 1: *Meta-analysis of SARS-CoV-2 proteomics studies reveals pathways consistently regulated across species and cell types.* A) Schematic of experimental design. B) Average of protein groups and of phosphorylation site groups quantified in each condition. Error bars are standard deviation. C) Number of differentially expressed protein groups and phosphorylation site groups for SARS-CoV-2 infected cells fold over mock-infected cells D) Pairwise Pearson coefficients of protein abundance log_2fold-change profiles from this study and published studies indicated. E) Kinase activity analysis based on log_2fold-change profiles from this study and published studies indicated. The absolute value of the normalized enrichment score (NES) is indicated by node sizes and the -Log_{10}(p-value) is indicated by the color scale. Decreases in kinase activity are indicated by negative -LogP values. F) Z-score-transformed log_2fold-change profiles of p38/MAPK kinases p38α and MK2 in this study and published studies indicated. Each row represents a protein substrate of the respective kinase with the maximum log_2fold-change of all phosphorylation sites each substrate indicated by the color scale.

Figure S1: A) Pairwise Pearson coefficients of phosphorylation group log_2fold-change profiles from this study and published studies indicated. B) Pairwise Pearson coefficients of kinase activities based on phosphorylation group log_2fold-change profiles from this study and published studies indicated. C) Z-score-transformed log_2fold-change profiles of top 10 regulated kinases (not including p38α and MK2 (Figure 1F)) in this study and published studies indicated. Each row represents a protein substrate of the respective kinase with the maximum log_2fold-change of all phosphorylation sites each substrate indicated by the color scale. D) Kinase activity estimates based on phosphorylation log_2fold-change profiles from this study and published studies indicated. E) Gene ontology enrichment analysis of protein abundance and phosphorylation site log_2fold-change profiles from this study and published studies indicated.

Figure 2: *Multiple components of the p38/MAPK pathway impact SARS-CoV-2 infection in human lung epithelial cells.* A) Schematic of p38/MAPK pathway. B) SARS-CoV-2 N infection rates normalized to siNTC treated/SARS-CoV-2 infected for each p38 isoform or downstream kinase siRNA target condition after SARS-CoV-2 MOI 0.1 for 36h in ACE2-A549. C) SARS-CoV-2 titer of supernatant from cells treated with siRNA targeting each p38 isoform or downstream kinase and infected with SARS-CoV-2 MOI 0.1 for 36h. D) Western blot of lysates collected in parallel with cells from 2B. E) SARS-CoV-2 infection rates normalized to siNTC treated/SARS-CoV-2 infected after SARS-CoV-2 MOI 0.1 for 36h in ACE2-A549 for each MAPKKK siRNA transfection. F) SARS-CoV-2 titer of supernatant from cells infected with SARS-CoV-2 MOI 0.1 for 36h in ACE2-A549 for each proviral MAPKKK siRNA transfection; all p-value annotations were calculated using a two-tailed paired student's t-test comparing each condition to siNTC/SARS-CoV-2 infected; NS = p-value > 0.05, * = 0.05 < p-value < 0.005, ** = 0.005 < p-value < 0.0005, *** = p-value < 0.0005

Supplemental Figure 2: A) Cell viability normalized to siNTC, p-values annotated for each condition compared to siNTC; all p-value annotations were calculated using a two-tailed paired student's t-test; NS = p-value > 0.05, * = 0.05 < p-value < 0.005, ** = 0.005 < p-value < 0.0005, *** = p-value < 0.0005

Figure 3: *p38ß proviral mechanism is primarily STAT1-independent but leads to ISG expression as a byproduct* A) ACE2-A549 cells were transfected with siNTC, sip38ß, sip38δ, or siMSK2 in biological quadruplicate and 48h

3 later infected with SARS-CoV-2 MOI 0.1 or mock-infected for 36h. Cells were then lysed and trypsin digested. A
4 fraction was saved for total protein abundance analysis and rest was subjected to phosphopeptide enrichment.
5 Mass spectrometry was performed using a DDA/DIA approach. Analysis was performed on raw data using
6 Spectronaut and MSstats. Significantly changing amount of protein groups or phosphopeptide groups defined
7 as $|\log_2$fold-change$| > 1$ and p-value < 0.05. B) Number of protein groups and number of phosphopeptide groups
8 identified in each biological replicate C) Number of significantly differentially expressed protein groups and
9 phosphopeptide groups for SARS-CoV-2 infected, sip38ß, sip38δ or siMSK2n fold over siNTC/SARS-CoV-2
0 infected and siNTC/SARS-CoV-2 infected fold over siNTC/mock-infected D) GO terms enriched in each condition
1 E) Heatmap of $\log_2$fold-changes for each ISG in each condition F) SARS-CoV-2 N protein expression from
2 immunofluorescence microscopy normalized to siNTC/SARS-CoV-2 infected for each p38 or downstream kinase
3 siRNA target condition in ACE2-A549 cells or ACE2-A549ΔSTAT1 cells after 30h SARS-CoV-2 infection. p-
4 values annotated for each siRNA condition between cell types calculated using a two-tailed paired student's t-
5 test, NS = p-value > 0.05, * = 0.05 < p-value < 0.005, ** = 0.005 < p-value < 0.0005, *** = p-value < 0.0005 G)
6 Western blot of lysates collected in parallel with cells from 2F
7
8 Supplemental Figure 3: A) Principal component analysis of protein abundance mass spectrometry samples B)
9 Principal component analysis of phosphopeptide-enriched mass spectrometry samples C) Heatmap of
0 Pearson's correlation analysis of protein abundance mass spectrometry samples D) Heatmap of Pearson's
1 correlation analysis of phosphopeptide-enriched mass spectrometry samples E) MS intensities of each sample
2 for protein abundance samples F) MS intensities of each sample for phosphopeptide-enriched samples G)
3 Western blot of lysates from cells transfected with siRNA targeting each gene of interest and infected with SARS-
4 CoV-2 MOI 0.1 30h in ACE2-A549 cells
5
6 Figure 4: *Phosphoproteome analysis reveals novel p38ß substrates* A) ACE2-A549 cells were pretreated with
7 DMSO, 1uM, or 10μMSB203580 for 1h in biological triplicate and infected with SARS-CoV-2 MOI 0.1 or mock-
8 infected for 24h. Or, ACE2-A549 cells were infected with SARS-CoV-2 MOI 0.1 or mock-infected for 24h and
9 terminally treated with DMSO or 10μMSB203580 in biological quadruplicate. Cells from both experiments were
0 then lysed and trypsin digested. A fraction was saved for total protein abundance analysis and rest was subjected

to phosphopeptide enrichment. Mass spectrometry was performed using a DDA/DIA approach. Analysis was performed on raw data using Spectronaut and MSstats. Significantly changing amount of phosphopeptide groups defined as ($|\log_2 \text{fold-change}| > 1$ and p-value < 0.05. B) Number of protein groups and number of phosphopeptide groups identified in each sample C) Number of significantly differentially expressed protein groups and phosphopeptide groups for SARS-CoV-2 infected/DMSO-pretreated fold over mock-infected/DMSO-pretreated and SARS-CoV-2 infected/1μMor 10μMSB203580-pretreated fold over SARS-CoV-2 infected/DMSO-pretreated and SARS-CoV-2 infected/DMSO terminally-treated fold over mock-infected/DMSO terminally-treated and SARS-CoV-2 infected/10μMSB203580 terminally-treated fold over SARS-CoV-2 infected/DMSO terminally-treated D) Heatmap of $\log_2$fold-changes for differentially expressed phosphopeptide groups in each condition, hierarchically clustered; cluster of interest in black box E) -log(p-value) of each highest -log(p-value) cluster from each group F) Log_2fold-changes of phosphopeptide groups (grey line) in cluster-of-interest for each condition; red line is trend overall of all phosphopeptide groups in cluster-of-interest G) Map of novel putative p38ß substrates identified in the cluster-of-interest; *-annotated proteins are known p38ß substrates

Supplemental Figure 4: A) Principal component analysis of protein abundance mass spectrometry samples from pre-treatment experiment B) Principal component analysis of phosphopeptide-enriched mass spectrometry samples from pre-treatment experiment C) Heatmap of Pearson's correlation analysis of protein abundance mass spectrometry samples from pre-treatment experiment D) Heatmap of Pearson's correlation analysis of phosphopeptide-enriched mass spectrometry samples from pre-treatment experiment E) MS intensities of each sample for protein abundance samples from pre-treatment experiment F) MS intensities of each sample for phosphopeptide-enriched samples from pre-treatment experiment G) Log_2Intensities of known p38ß substrates from pre-treatment experiment H) GO terms enriched for cluster-of-interest proteins I) Principal component analysis of protein abundance mass spectrometry samples from terminally-treated experiment J) Principal component analysis of phosphopeptide-enriched mass spectrometry samples from terminally-treated experiment K) Heatmap of Pearson's correlation analysis of protein abundance mass spectrometry samples from terminally-treated experiment L) Heatmap of Pearson's correlation analysis of phosphopeptide-enriched mass spectrometry samples from terminally-treated experiment M) MS intensities of each sample for protein

abundance samples from terminally-treated experiment N) MS intensities of each sample for phosphopeptide-enriched samples from terminally-treated experiment O) Log_2Intensities of known p38ß substrates from terminally-treated experiment

Figure 5: *p38ß promotes viral protein translation* A) Plot of log_2fold-changes of each phosphopeptide group on SARS-CoV-2 N differentially expressed for SARS-CoV-2 infected/10μMSB203580 terminally-treated fold over SARS-CoV-2 infected/DMSO terminally-treated; entropy indicated as yellow line B) Log_2intensities of total N protein abundance from terminally-treated experiment (Figure 4A); NS = p-value > 0.05 C) Number of viral reads at each nucleotide in SARS-CoV-2 genome from mRNA-Seq; schematic of genome beneath D) Percent viral reads from mRNA-Seq of ACE2-A549 cells transfected with siNTC or sip38ß and infected with SARS-CoV-2 MOI 0.75 or mock-infected for 8 hours; significance annotated as p-value from two-tailed student's t-test, NS = p-value > 0.05; western blot from lysates collected in parallel E) GO terms enriched for siMAPK11/SARS-CoV-2 infected fold-over siNTC/SARS-CoV-2 infected differentially expressed genes; downregulated GO terms have a negative -log(p-value) for the fill F) SARS-CoV-2 N protein expression normalized or transcript expression normalized to siNTC treated/SARS-CoV-2 infected for each kinase siRNA target condition in cells infected with SARS-CoV-2 MOI 2 for 8 hours, p-value annotations were calculated using a two-tailed paired student's t-test, NS = p-value > 0.05, * = 0.05 < p-value < 0.005, ** = 0.005 < p-value < 0.0005, *** = p-value < 0.0005

Supplemental Figure 5: A) Log_2intensities of each significantly differentially expressed phosphopeptide group on SARS-CoV-2 N from terminally-treated experiment (Figure 4A) B) SARS-CoV-2 N protein expression normalized or transcript expression normalized to siNTC treated/SARS-CoV-2 infected for each kinase siRNA target condition in cells infected with SARS-CoV-2 MOI 2 for 8 hours; p-value annotations were calculated using a two-tailed paired student's t-test, NS = p-value > 0.05, * = 0.05 < p-value < 0.005, ** = 0.005 < p-value < 0.0005, *** = p-value < 0.0005 C) GO terms enriched for siNTC/SARS-CoV-2 infected fold-over siNTC/mock-infected differentially expressed genes; downregulated GO terms have a negative -log(p-value) for the fill

Supplementary Table Legends

Table S1: Log_2fold-changes, p-values, and adjusted p-values for each protein group or phosphopeptide group detected, by condition, for the comparisons indicated. Tabs are separate experiments and annotated either protein abundance (AB) or phosphopeptide (PH)

Table S2: Gene set enrichment analysis results for kinase activity including kinase of interest, p-values, adjusted p-values, enrichment scores (ES), normalized enrichment scores (NES), number of substrates contributing (size), substrates contributing (leadingEdgeText), by condition, for comparison between the present study and other published SARS-CoV-2 phosphoproteomics studies (Figure 1E-F and S1C-D)

Table S3: Gene set enrichment analysis results for gene ontology (GO) including GO term (pathway), p-values, adjusted p-values, $-log_{10}$(p-value) (negative if negative NES), enrichment scores (ES), normalized enrichment scores (NES), number of proteins contributing (size), proteins contributing (leadingEdgeText), description of GO term (definition), by condition and type of MS analysis (protein abundance or phosphopeptide), for comparison between the present study and other published SARS-CoV-2 phosphoproteomics studies (Figure S1E)

Table S4: Z-score transformed log_2fold-changes for the top 10 regulated kinase substrates across studies. Values represent the phosphosite group with the maximum Z-score transformed log_2fold-change per substrate protein in each data set.

Table S5: Gene set enrichment analysis results for gene ontology (GO) including GO term (pathway), p-values, adjusted p-values, $-log_{10}$(p-value), enrichment scores (ES), normalized enrichment scores (NES), number of proteins contributing (size), description of GO term (definition), by condition, for siRNA MS experiment (Figure 3)

Table S6: Log_2fold-changes for each phosphopeptide group identified as a novel, putative p38ß substrate, by condition; known substrates annotated (Figure 4F-G).

Table S7: Log_2fold-changes, p-values, and adjusted p-values for differential expression results from mRNA-Seq experiment; tabs specify conditions (Figure 5).

Table S8: Gene ontology (GO) enrichment analysis of differential gene expression results from mRNA-Seq experiment comparing SARS-CoV-2-infected/p38β knockdown to SARS-CoV-2-infected/non-targeting control, including Z score, combined score, p-values, genes contributing (overlapping genes), $-log_{10}$(p-value), and if decreasing or increasing; tabs indicate conditions

Table S9: Gene ontology (GO) enrichment analysis of differential gene expression results from mRNA-Seq experiment comparing SARS-CoV-2-infected to mock-infected cells, including Z score, combined score, p-values, genes contributing (overlapping genes), $-\log_{10}$(p-value), and if decreasing or increasing; tabs indicate conditions

References

Aydillo, T., Ayllon, J., Pavlisin, A., Martinez-Romero, C., Tripathi, S., Mena, I., Moreira-Soto, A., Vicente-Santos, A., Corrales-Aguilar, E., Schwemmle, M.*, et al.* (2018). Specific Mutations in the PB2 Protein of Influenza A Virus Compensate for the Lack of Efficient Interferon Antagonism of the NS1 Protein of Bat Influenza A-Like Viruses. J Virol *92*.

Banerjee, S., Narayanan, K., Mizutani, T., and Makino, S. (2002). Murine coronavirus replication-induced p38 mitogen-activated protein kinase activation promotes interleukin-6 production and virus replication in cultured cells. J Virol *76*, 5937-5948.

Beardmore, V.A., Hinton, H.J., Eftychi, C., Apostolaki, M., Armaka, M., Darragh, J., McIlrath, J., Carr, J.M., Armit, L.J., Clacher, C.*, et al.* (2005). Generation and characterization of p38beta (MAPK11) gene-targeted mice. Mol Cell Biol *25*, 10454-10464.

Beenstock, J., Melamed, D., Mooshayef, N., Mordechay, D., Garfinkel, B.P., Ahn, N.G., Admon, A., and Engelberg, D. (2016). p38beta Mitogen-Activated Protein Kinase Modulates Its Own Basal Activity by Autophosphorylation of the Activating Residue Thr180 and the Inhibitory Residues Thr241 and Ser261. Mol Cell Biol *36*, 1540-1554.

Beltrao, P., Albanese, V., Kenner, L.R., Swaney, D.L., Burlingame, A., Villen, J., Lim, W.A., Fraser, J.S., Frydman, J., and Krogan, N.J. (2012). Systematic functional prioritization of protein posttranslational modifications. Cell *150*, 413-425.

Benjamini, Y., and Hochberg, Y. (1995). Controlling the False Discovery Rate - a Practical and Powerful Approach to Multiple Testing. J R Stat Soc B *57*, 289-300.

Bojkova, D., Klann, K., Koch, B., Widera, M., Krause, D., Ciesek, S., Cinatl, J., and Munch, C. (2020). Proteomics of SARS-CoV-2-infected host cells reveals therapy targets. Nature *583*, 469-472.

Bouhaddou, M., Memon, D., Meyer, B., White, K.M., Rezelj, V.V., Correa Marrero, M., Polacco, B.J., Melnyk, J.E., Ulferts, S., Kaake, R.M.*, et al.* (2020). The Global Phosphorylation Landscape of SARS-CoV-2 Infection. Cell *182*, 685-712 e619.

Bruderer, R., Bernhardt, O.M., Gandhi, T., Xuan, Y., Sondermann, J., Schmidt, M., Gomez-Varela, D., and Reiter, L. (2017). Optimization of Experimental Parameters in Data-Independent Mass Spectrometry Significantly Increases Depth and Reproducibility of Results. Mol Cell Proteomics *16*, 2296-2309.

Chang, C.K., Hou, M.H., Chang, C.F., Hsiao, C.D., and Huang, T.H. (2014). The SARS coronavirus nucleocapsid protein--forms and functions. Antiviral Res *103*, 39-50.

Chen, H., Gill, A., Dove, B.K., Emmett, S.R., Kemp, C.F., Ritchie, M.A., Dee, M., and Hiscox, J.A. (2005). Mass spectroscopic characterization of the coronavirus infectious bronchitis virus nucleoprotein and elucidation of the role of phosphorylation in RNA binding by using surface plasmon resonance. J Virol *79*, 1164-1179.

Choi, M., Chang, C.Y., Clough, T., Broudy, D., Killeen, T., MacLean, B., and Vitek, O. (2014). MSstats: an R package for statistical analysis of quantitative mass spectrometry-based proteomic experiments. Bioinformatics *30*, 2524-2526.

Cuenda, A., Rouse, J., Doza, Y.N., Meier, R., Cohen, P., Gallagher, T.F., Young, P.R., and Lee, J.C. (1995). SB 203580 is a specific inhibitor of a MAP kinase homologue which is stimulated by cellular stresses and interleukin-1. FEBS Lett *364*, 229-233.

Daniloski, Z., Jordan, T.X., Wessels, H.H., Hoagland, D.A., Kasela, S., Legut, M., Maniatis, S., Mimitou, E.P., Lu, L., Geller, E.*, et al.* (2021). Identification of Required Host Factors for SARS-CoV-2 Infection in Human Cells. Cell *184*, 92-105 e116.

Grein, J., Ohmagari, N., Shin, D., Diaz, G., Asperges, E., Castagna, A., Feldt, T., Green, G., Green, M.L., Lescure, F.X.*, et al.* (2020). Compassionate Use of Remdesivir for Patients with Severe Covid-19. N Engl J Med *382*, 2327-2336.

Group, R.C., Horby, P., Lim, W.S., Emberson, J.R., Mafham, M., Bell, J.L., Linsell, L., Staplin, N., Brightling, C., Ustianowski, A.*, et al.* (2020). Dexamethasone in Hospitalized Patients with Covid-19 - Preliminary Report. N Engl J Med.

Hadfield, J., Megill, C., Bell, S.M., Huddleston, J., Potter, B., Callender, C., Sagulenko, P., Bedford, T., and Neher, R.A. (2018). Nextstrain: real-time tracking of pathogen evolution. Bioinformatics *34*, 4121-4123.

Han, J., Wu, J., and Silke, J. (2020). An overview of mammalian p38 mitogen-activated protein kinases, central regulators of cell stress and receptor signaling. F1000Res *9*.

Hornbeck, P.V., Zhang, B., Murray, B., Kornhauser, J.M., Latham, V., and Skrzypek, E. (2015). PhosphoSitePlus, 2014: mutations, PTMs and recalibrations. Nucleic Acids Res *43*, D512-520.

Jimenez-Guardeno, J.M., Nieto-Torres, J.L., DeDiego, M.L., Regla-Nava, J.A., Fernandez-Delgado, R., Castano-Rodriguez, C., and Enjuanes, L. (2014). The PDZ-binding motif of severe acute respiratory syndrome coronavirus envelope protein is a determinant of viral pathogenesis. PLoS Pathog *10*, e1004320.

Karki, R., Sharma, B.R., Tuladhar, S., Williams, E.P., Zalduondo, L., Samir, P., Zheng, M., Sundaram, B., Banoth, B., Malireddi, R.K.S.*, et al.* (2021). Synergism of TNF-alpha and IFN-gamma Triggers Inflammatory Cell Death, Tissue Damage, and Mortality in SARS-CoV-2 Infection and Cytokine Shock Syndromes. Cell *184*, 149-168 e117.

Kopecky-Bromberg, S.A., Martinez-Sobrido, L., and Palese, P. (2006). 7a protein of severe acute respiratory syndrome coronavirus inhibits cellular protein synthesis and activates p38 mitogen-activated protein kinase. J Virol *80*, 785-793.

Lu, Y., Cai, H., Lu, M., Ma, Y., Li, A., Gao, Y., Zhou, J., Gu, H., Li, J., and Gu, J. (2020). Porcine Epidemic Diarrhea Virus Deficient in RNA Cap Guanine-N-7 Methylation Is Attenuated and Induces Higher Type I and III Interferon Responses. J Virol *94*.

Mehta, P., McAuley, D.F., Brown, M., Sanchez, E., Tattersall, R.S., Manson, J.J., and Hlh Across Speciality Collaboration, U.K. (2020). COVID-19: consider cytokine storm syndromes and immunosuppression. Lancet *395*, 1033-1034.

Merad, M., and Martin, J.C. (2020). Pathological inflammation in patients with COVID-19: a key role for monocytes and macrophages. Nat Rev Immunol *20*, 355-362.

Robinson, J.T., Thorvaldsdottir, H., Winckler, W., Guttman, M., Lander, E.S., Getz, G., and Mesirov, J.P. (2011). Integrative genomics viewer. Nat Biotechnol *29*, 24-26.

Rosas, I.O., Brau, N., Waters, M., Go, R.C., Hunter, B.D., Bhagani, S., Skiest, D., Aziz, M.S., Cooper, N., Douglas, I.S.*, et al.* (2021). Tocilizumab in Hospitalized Patients with Severe Covid-19 Pneumonia. N Engl J Med *384*, 1503-1516.

Roux, P.P., and Blenis, J. (2004). ERK and p38 MAPK-activated protein kinases: a family of protein kinases with diverse biological functions. Microbiol Mol Biol Rev *68*, 320-344.

Salama, C., Han, J., Yau, L., Reiss, W.G., Kramer, B., Neidhart, J.D., Criner, G.J., Kaplan-Lewis, E., Baden, R., Pandit, L.*, et al.* (2021). Tocilizumab in Patients Hospitalized with Covid-19 Pneumonia. N Engl J Med *384*, 20-30.

Schoggins, J.W., and Rice, C.M. (2011). Interferon-stimulated genes and their antiviral effector functions. Curr Opin Virol *1*, 519-525.

Seifert, L.L., Si, C., Saha, D., Sadic, M., de Vries, M., Ballentine, S., Briley, A., Wang, G., Valero-Jimenez, A.M., Mohamed, A.*, et al.* (2019). The ETS transcription factor ELF1 regulates a broadly antiviral program distinct from the type I interferon response. PLoS Pathog *15*, e1007634.

Stukalov, A., Girault, V., Grass, V., Karayel, O., Bergant, V., Urban, C., Haas, D.A., Huang, Y., Oubraham, L., Wang, A.*, et al.* (2021). Multilevel proteomics reveals host perturbations by SARS-CoV-2 and SARS-CoV. Nature.

Subramanian, A., Tamayo, P., Mootha, V.K., Mukherjee, S., Ebert, B.L., Gillette, M.A., Paulovich, A., Pomeroy, S.L., Golub, T.R., Lander, E.S.*, et al.* (2005). Gene set enrichment analysis: a knowledge-based approach for interpreting genome-wide expression profiles. Proc Natl Acad Sci U S A *102*, 15545-15550.

Wu, C.H., Chen, P.J., and Yeh, S.H. (2014). Nucleocapsid phosphorylation and RNA helicase DDX1 recruitment enables coronavirus transition from discontinuous to continuous transcription. Cell Host Microbe *16*, 462-472.

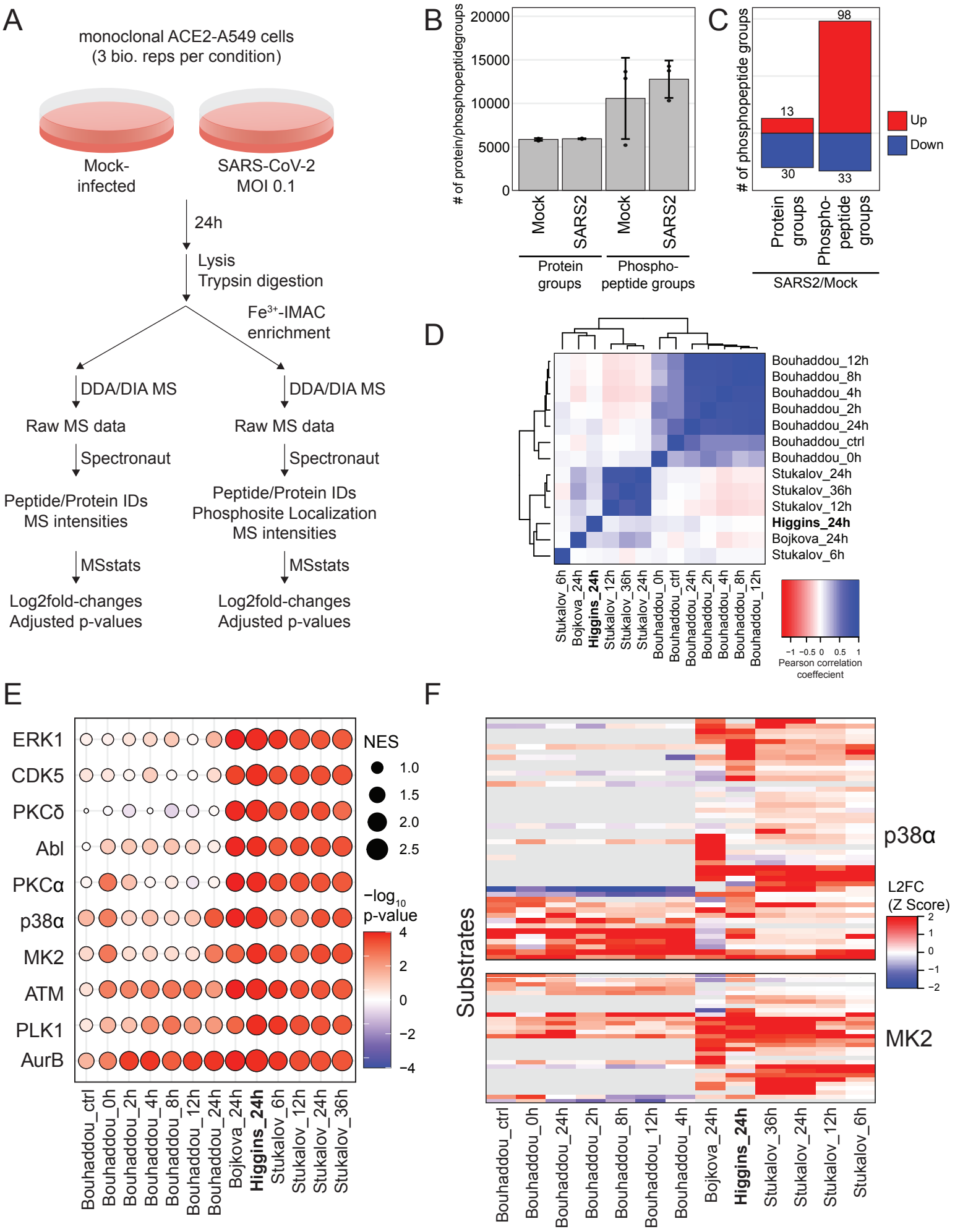
A
monoclonal ACE2-A549 cells
(3 bio. reps per condition)
Mock-infected
SARS-CoV-2 MOI 0.1
24h
Lysis
Trypsin digestion
Fe3+-IMAC enrichment
DDA/DIA MS
Raw MS data
Spectronaut
Peptide/Protein IDs
MS intensities
MSstats
Log2fold-changes
Adjusted p-values
Phosphosite Localization
B
# of protein/phosphopeptidegroups
Mock
SARS2
Protein groups
Phospho-peptide groups
C
# of phosphopeptide groups
98
13
30
33
Up
Down
SARS2/Mock
D
Bouhaddou_12h
Bouhaddou_8h
Bouhaddou_4h
Bouhaddou_2h
Bouhaddou_24h
Bouhaddou_ctrl
Bouhaddou_0h
Stukalov_24h
Stukalov_36h
Stukalov_12h
Higgins_24h
Bojkova_24h
Stukalov_6h
Pearson correlation coeffecient
E
ERK1
CDK5
PKCδ
Abl
PKCα
p38α
MK2
ATM
PLK1
AurB
NES
1.0
1.5
2.0
2.5
−log10 p-value
F
Substrates
p38α
MK2
L2FC (Z Score)

Figure 1

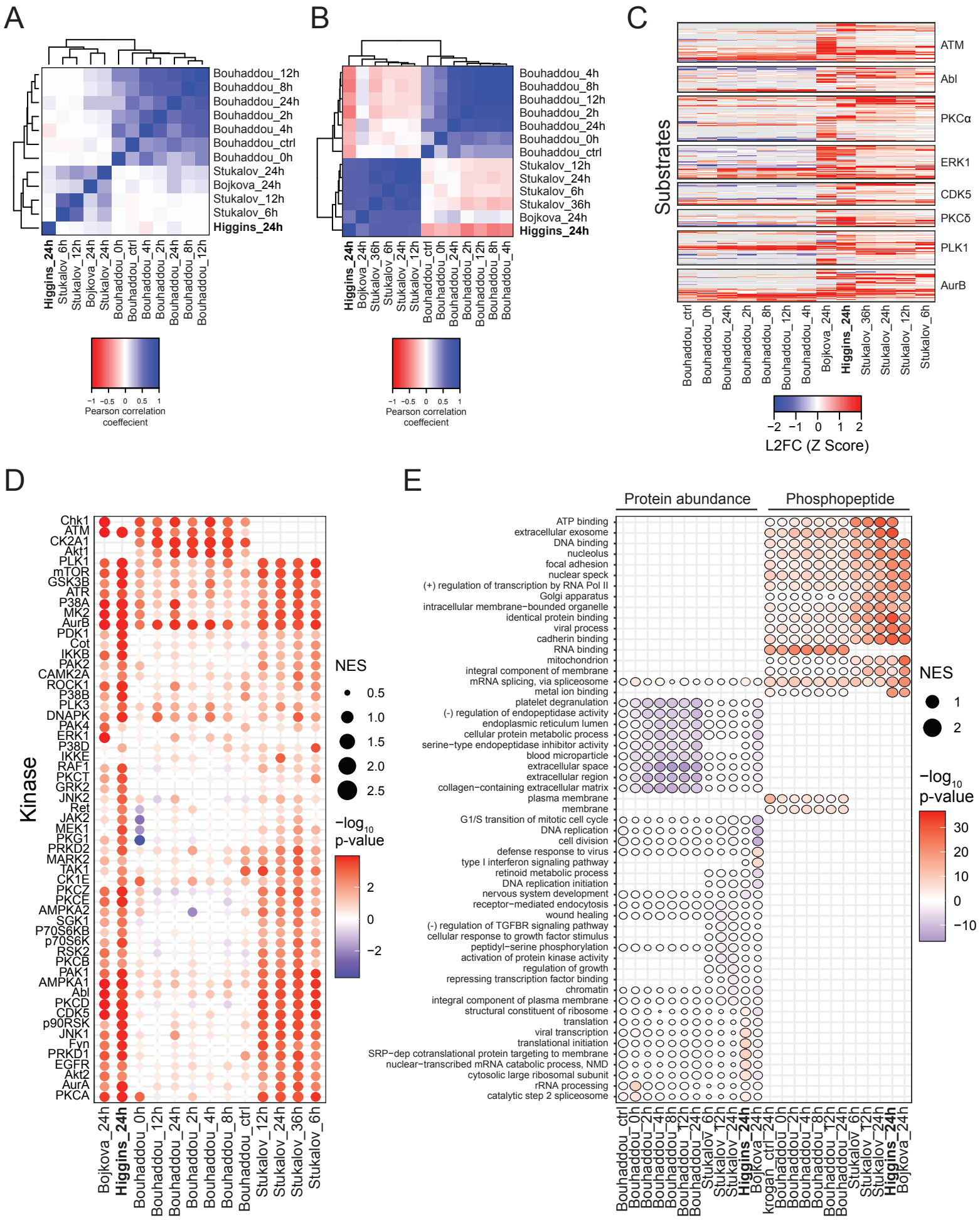

Supplemental Figure 1

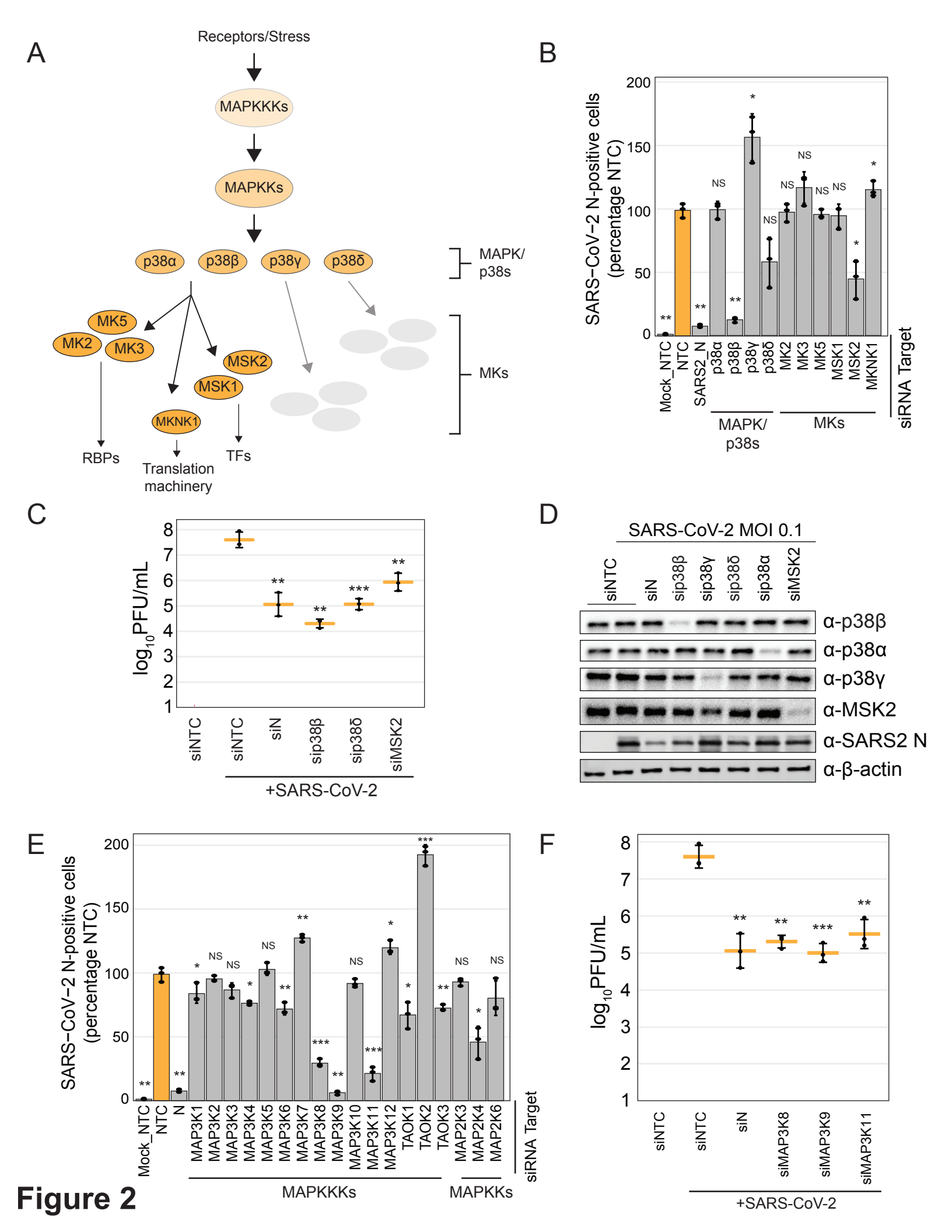
A
Receptors/Stress
MAPKKKs
MAPKKs
p38α
p38β
p38γ
p38δ
MAPK/ p38s
MK5
MK2
MK3
MSK2
MSK1
MKNK1
MKs
RBPs
Translation machinery
TFs
B
SARS−CoV−2 N-positive cells (percentage NTC)
Mock_NTC
NTC
SARS2_N
p38α
p38β
p38γ
p38δ
MK2
MK3
MK5
MSK1
MSK2
MKNK1
MAPK/ p38s
MKs
siRNA Target
C
log10PFU/mL
siNTC
siNTC
siN
sip38β
sip38δ
siMSK2
+SARS-CoV-2
D
SARS-CoV-2 MOI 0.1
siNTC
siN
sip38β
sip38γ
sip38δ
sip38α
siMSK2
α-p38β
α-p38α
α-p38γ
α-MSK2
α-SARS2 N
α-β-actin
E
SARS−CoV−2 N-positive cells (percentage NTC)
Mock_NTC
NTC
N
MAP3K1
MAP3K2
MAP3K3
MAP3K4
MAP3K5
MAP3K6
MAP3K7
MAP3K8
MAP3K9
MAP3K10
MAP3K11
MAP3K12
TAOK1
TAOK2
TAOK3
MAP2K3
MAP2K4
MAP2K6
MAPKKKs
MAPKKs
siRNA Target
F
log10PFU/mL
siNTC
siNTC
siN
siMAP3K8
siMAP3K9
siMAP3K11
+SARS-CoV-2

Figure 2

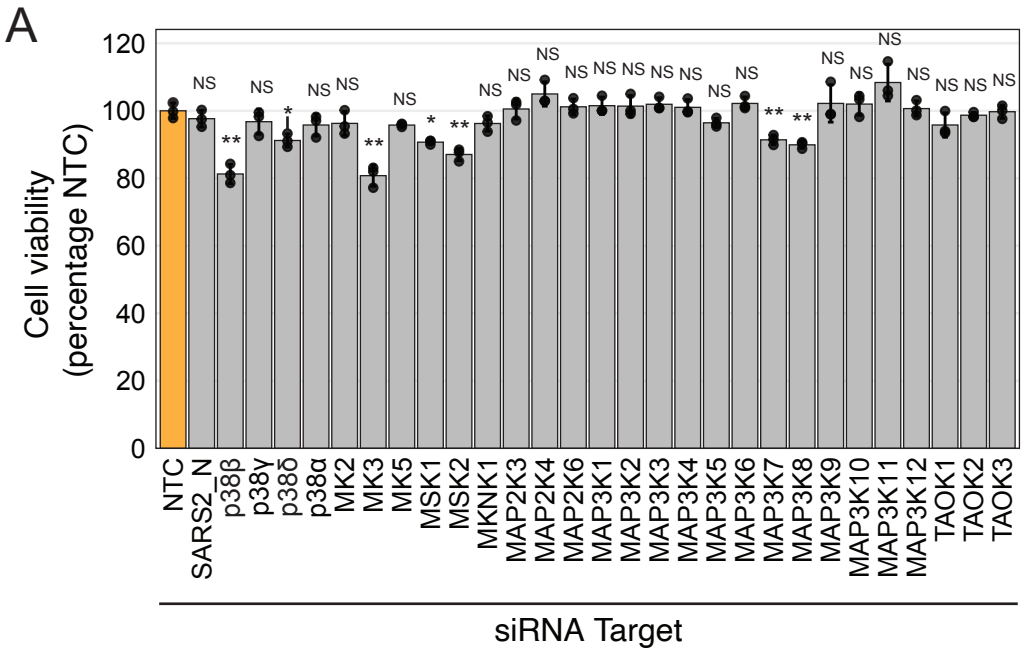

Supplemental Figure 2

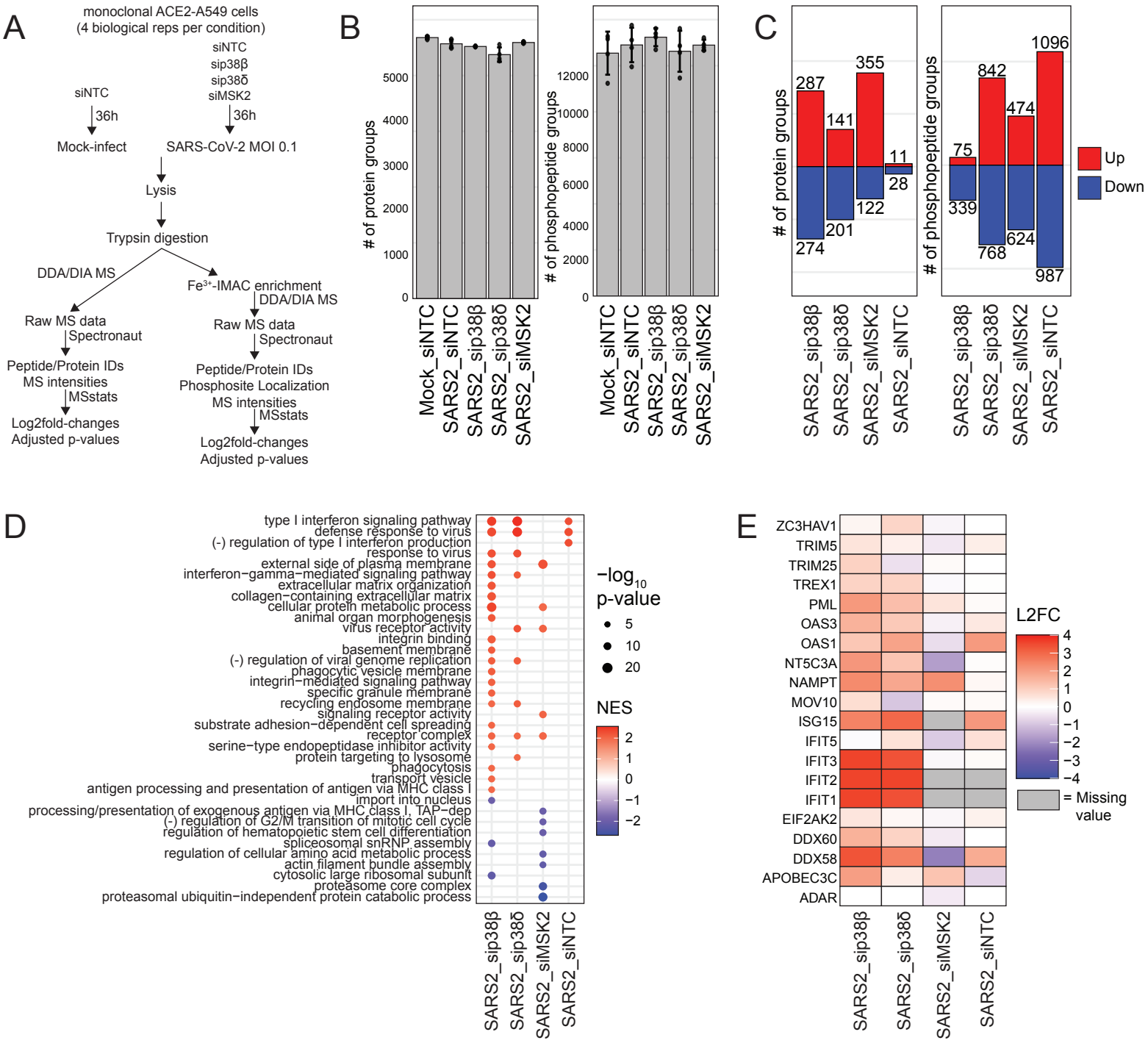
A
monoclonal ACE2-A549 cells
(4 biological reps per condition)
siNTC
siNTC
sip38β
sip38δ
siMSK2
36h
36h
Mock-infect
SARS-CoV-2 MOI 0.1
Lysis
Trypsin digestion
DDA/DIA MS
Fe3+-IMAC enrichment
DDA/DIA MS
Raw MS data
Spectronaut
Raw MS data
Spectronaut
Peptide/Protein IDs
MS intensities
MSstats
Log2fold-changes
Adjusted p-values
Peptide/Protein IDs
Phosphosite Localization
MS intensities
MSstats
Log2fold-changes
Adjusted p-values
B
# of protein groups
# of phosphopeptide groups
Mock_siNTC
SARS2_siNTC
SARS2_sip38β
SARS2_sip38δ
SARS2_siMSK2
C
# of protein groups
# of phosphopeptide groups
287
141
355
11
274
201
122
28
75
842
1096
339
768
474
624
987
Up
Down
SARS2_sip38β
SARS2_sip38δ
SARS2_siMSK2
SARS2_siNTC
D
type I interferon signaling pathway
defense response to virus
(-) regulation of type I interferon production
response to virus
external side of plasma membrane
interferon-gamma-mediated signaling pathway
extracellular matrix organization
collagen-containing extracellular matrix
cellular protein metabolic process
animal organ morphogenesis
virus receptor activity
integrin binding
basement membrane
(-) regulation of viral genome replication
phagocytic vesicle membrane
integrin-mediated signaling pathway
specific granule membrane
recycling endosome membrane
signaling receptor activity
substrate adhesion-dependent cell spreading
receptor complex
serine-type endopeptidase inhibitor activity
protein targeting to lysosome
phagocytosis
transport vesicle
antigen processing and presentation of antigen via MHC class I
import into nucleus
processing/presentation of exogenous antigen via MHC class I, TAP-dep
(-) regulation of G2/M transition of mitotic cell cycle
regulation of hematopoietic stem cell differentiation
spliceosomal snRNP assembly
regulation of cellular amino acid metabolic process
actin filament bundle assembly
cytosolic large ribosomal subunit
proteasome core complex
proteasomal ubiquitin-independent protein catabolic process
−log10 p-value
NES
SARS2_sip38β
SARS2_sip38δ
SARS2_siMSK2
SARS2_siNTC
E
ZC3HAV1
TRIM5
TRIM25
TREX1
PML
OAS3
OAS1
NT5C3A
NAMPT
MOV10
ISG15
IFIT5
IFIT3
IFIT2
IFIT1
EIF2AK2
DDX60
DDX58
APOBEC3C
ADAR
L2FC
= Missing value
SARS2_sip38β
SARS2_sip38δ
SARS2_siMSK2
SARS2_siNTC
F
SARS−CoV−2 N-positive cells (percentage NTC)
Cell Type
WT
STAT1-/-
NS
*
siNTC
siNTC
sip38β
sipp38γ
sip38δ
sip38α
siMSK2
siN
SARS-CoV-2 (MOI 0.1, 30h)
G
SARS-CoV-2 (MOI 0.1, 30h)
siNTC
siN
sip38β
sip38γ
sip38δ
sip38α
siMSK2
STAT1
WT
KO
α-SARS2 N
α-MX1
α-(P)-STAT1
α-STAT1
α-p38β
α-p38α
α-MSK2
α-β-actin

Figure 3

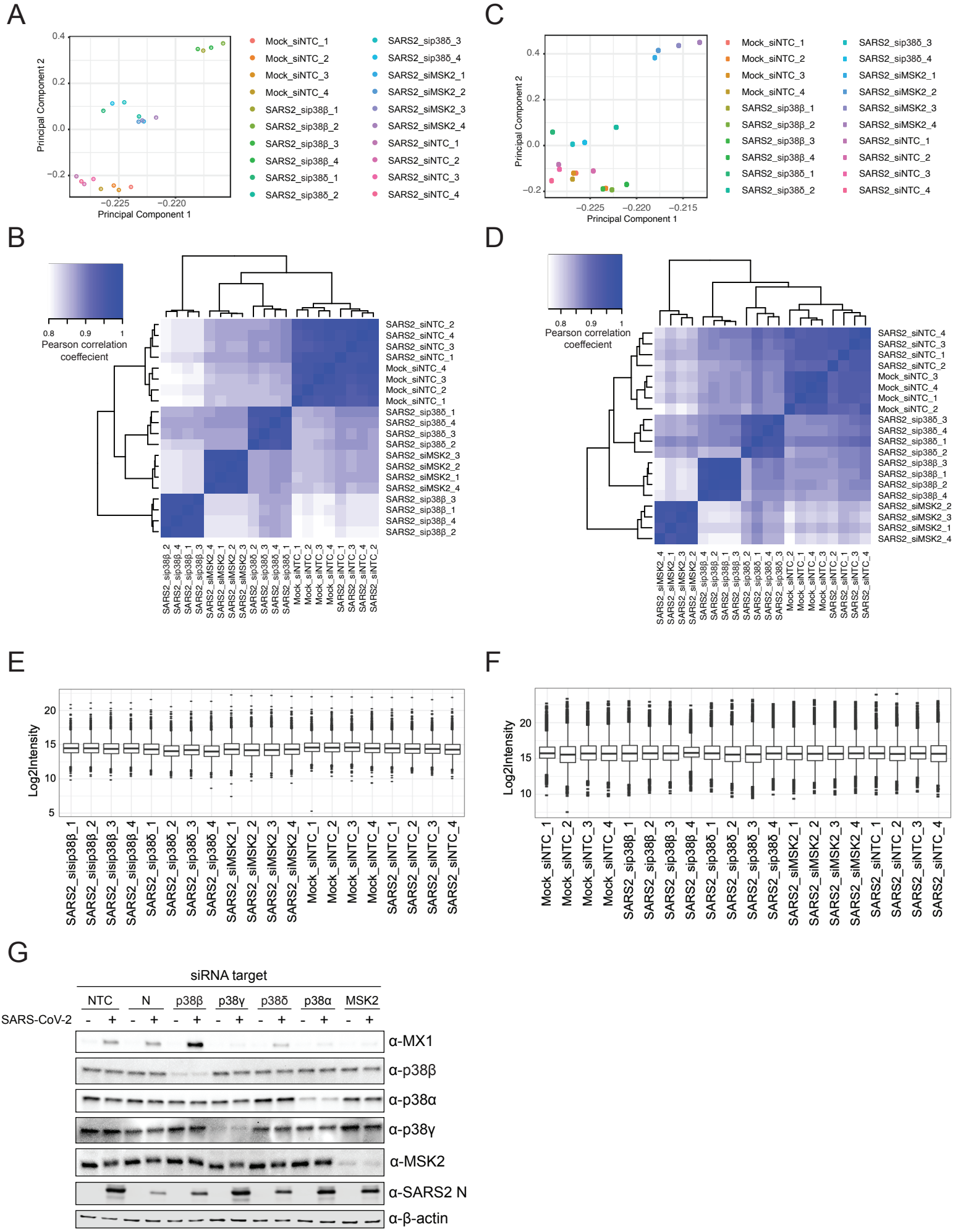

Supplemental Figure 3

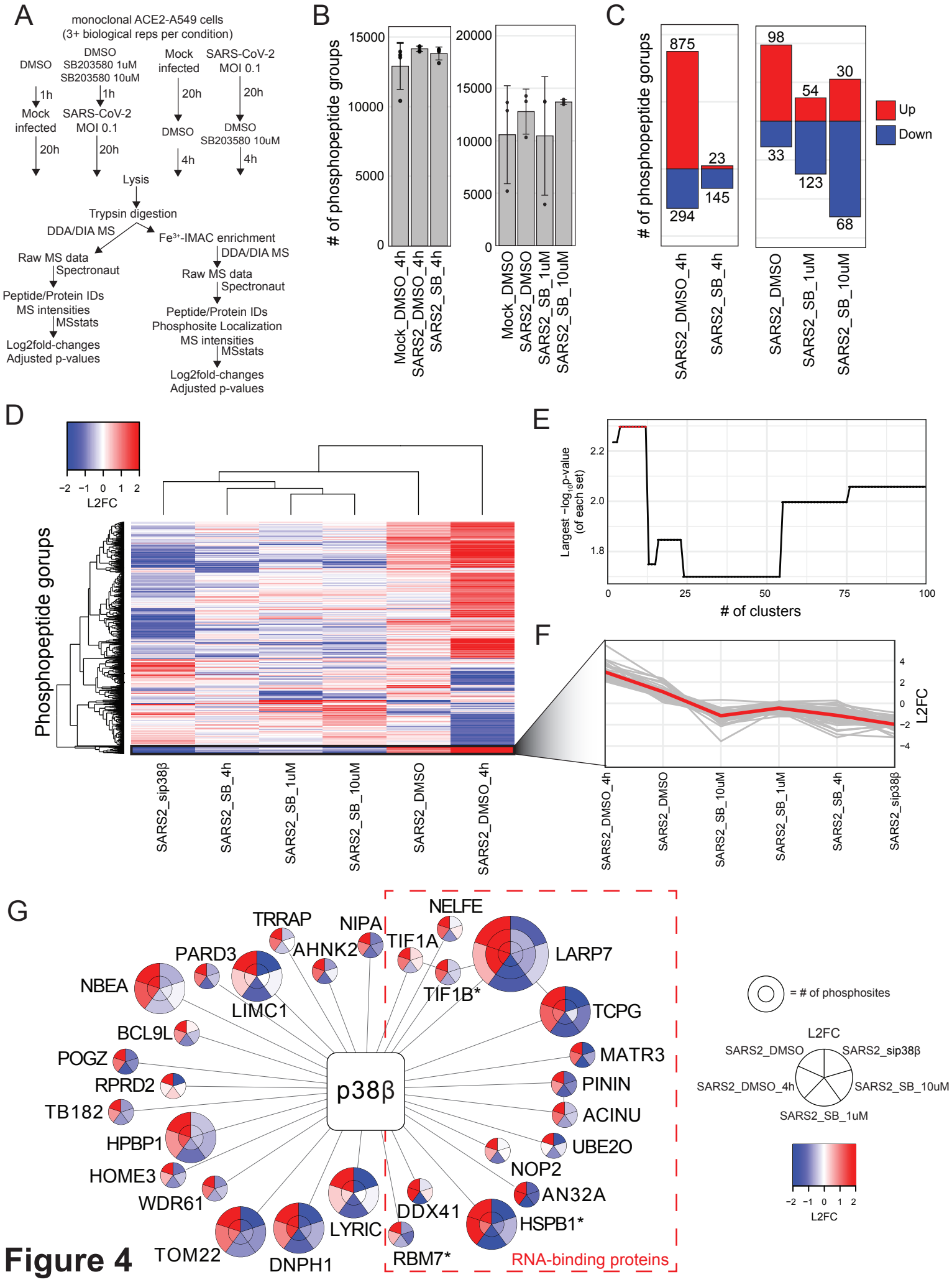
A
monoclonal ACE2-A549 cells
(3+ biological reps per condition)
DMSO
DMSO
SB203580 1uM
SB203580 10uM
Mock infected
SARS-CoV-2 MOI 0.1
1h
20h
4h
Lysis
Trypsin digestion
DDA/DIA MS
Fe3+-IMAC enrichment
Raw MS data
Spectronaut
Peptide/Protein IDs
MS intensities
MSstats
Phosphosite Localization
Log2fold-changes
Adjusted p-values
B
# of phosphopeptide groups
Mock_DMSO_4h
SARS2_DMSO_4h
SARS2_SB_4h
Mock_DMSO
SARS2_DMSO
SARS2_SB_1uM
SARS2_SB_10uM
C
875
294
23
145
98
33
54
123
30
68
Up
Down
D
L2FC
Phosphopeptide gorups
SARS2_sip38β
SARS2_SB_4h
SARS2_SB_1uM
SARS2_SB_10uM
SARS2_DMSO
SARS2_DMSO_4h
E
Largest −log10 p-value (of each set)
# of clusters
F
L2FC
G
p38β
TRRAP
NIPA
AHNK2
PARD3
NBEA
LIMC1
BCL9L
POGZ
RPRD2
TB182
HPBP1
HOME3
WDR61
TOM22
DNPH1
LYRIC
RBM7*
DDX41
HSPB1*
AN32A
NOP2
UBE2O
ACINU
PININ
MATR3
TCPG
LARP7
TIF1B*
TIF1A
NELFE
RNA-binding proteins
= # of phosphosites
L2FC
SARS2_DMSO
SARS2_sip38β
SARS2_DMSO_4h
SARS2_SB_10uM
SARS2_SB_1uM

Figure 4

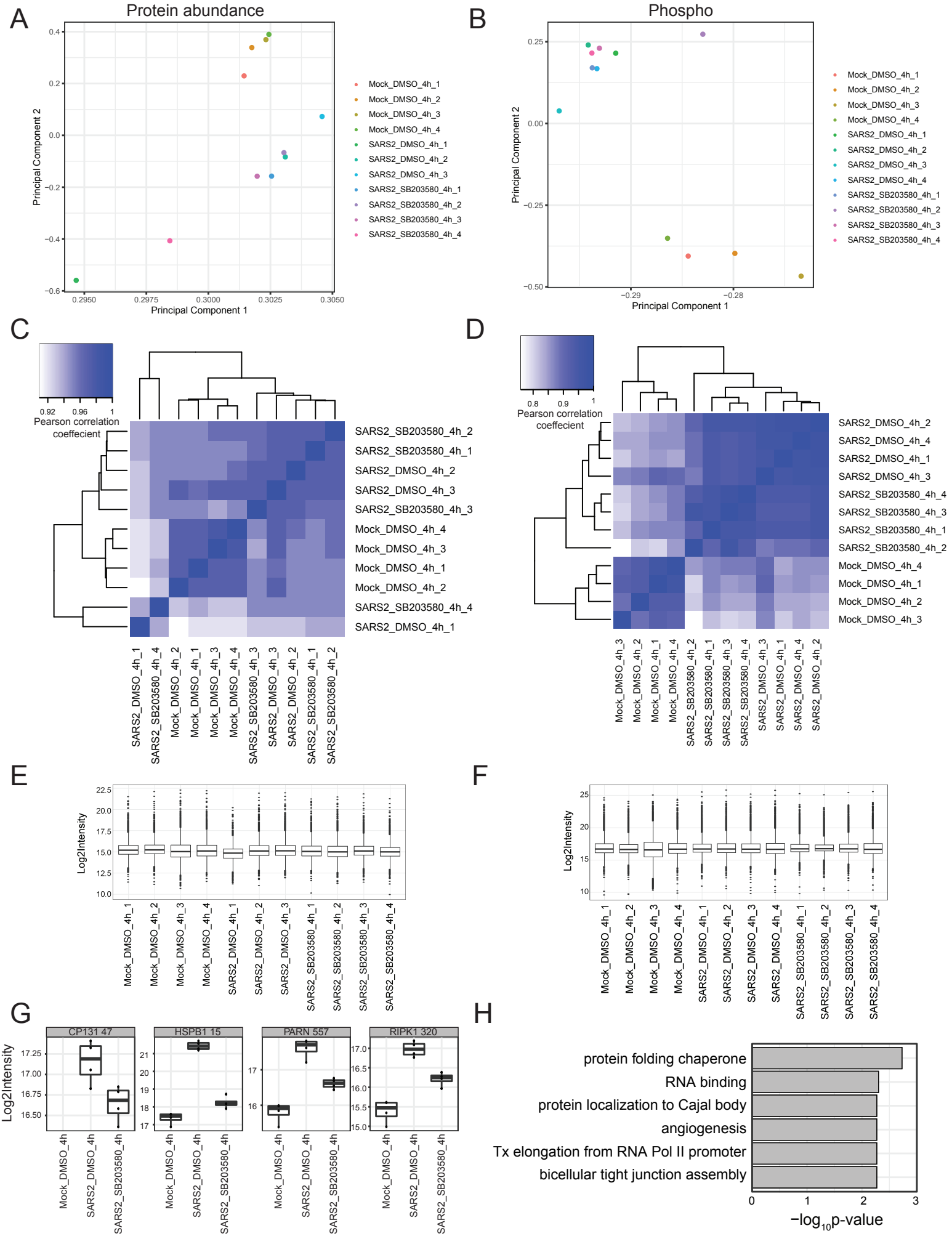

Supplemental Figure 4

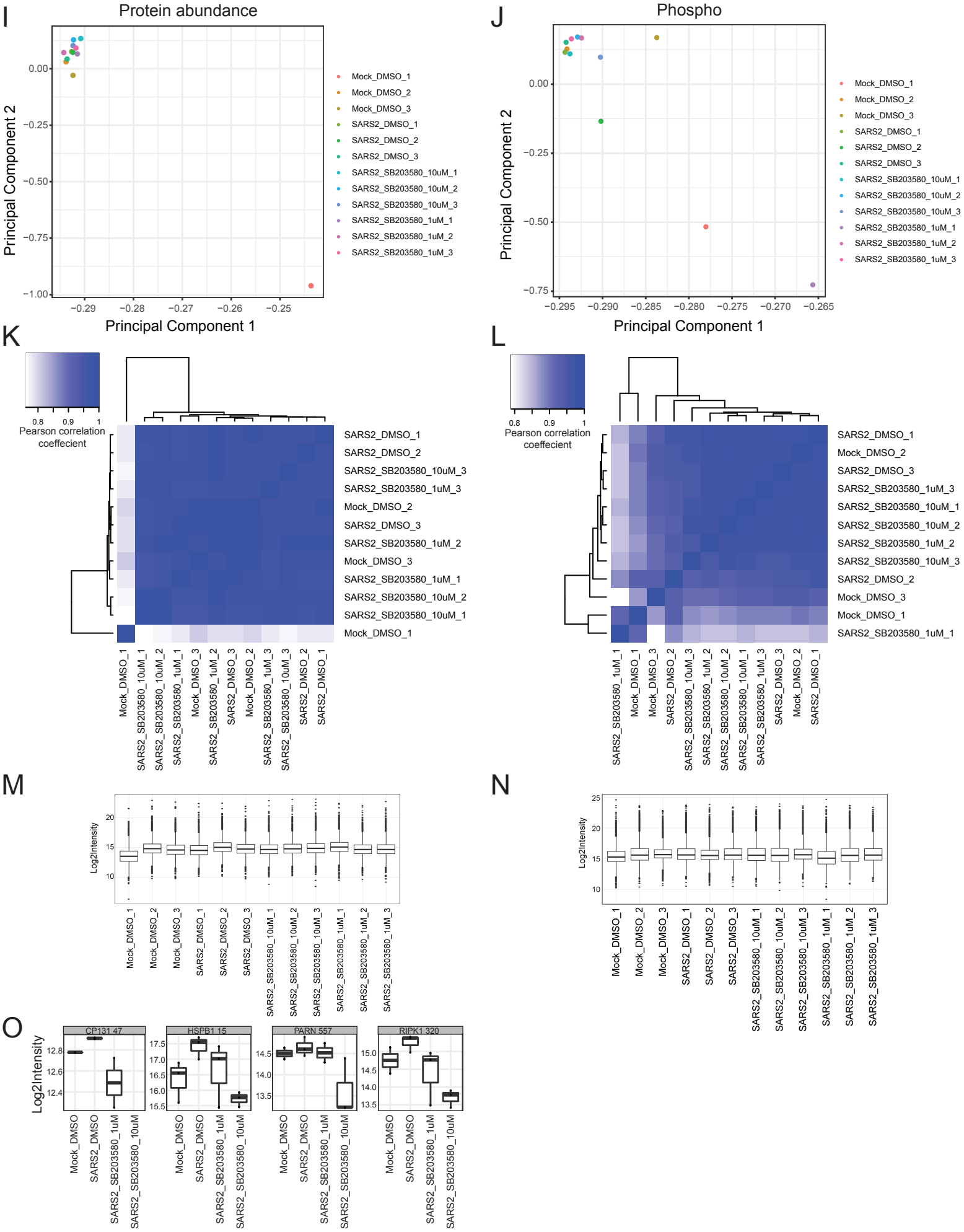

Supplemental Figure 4

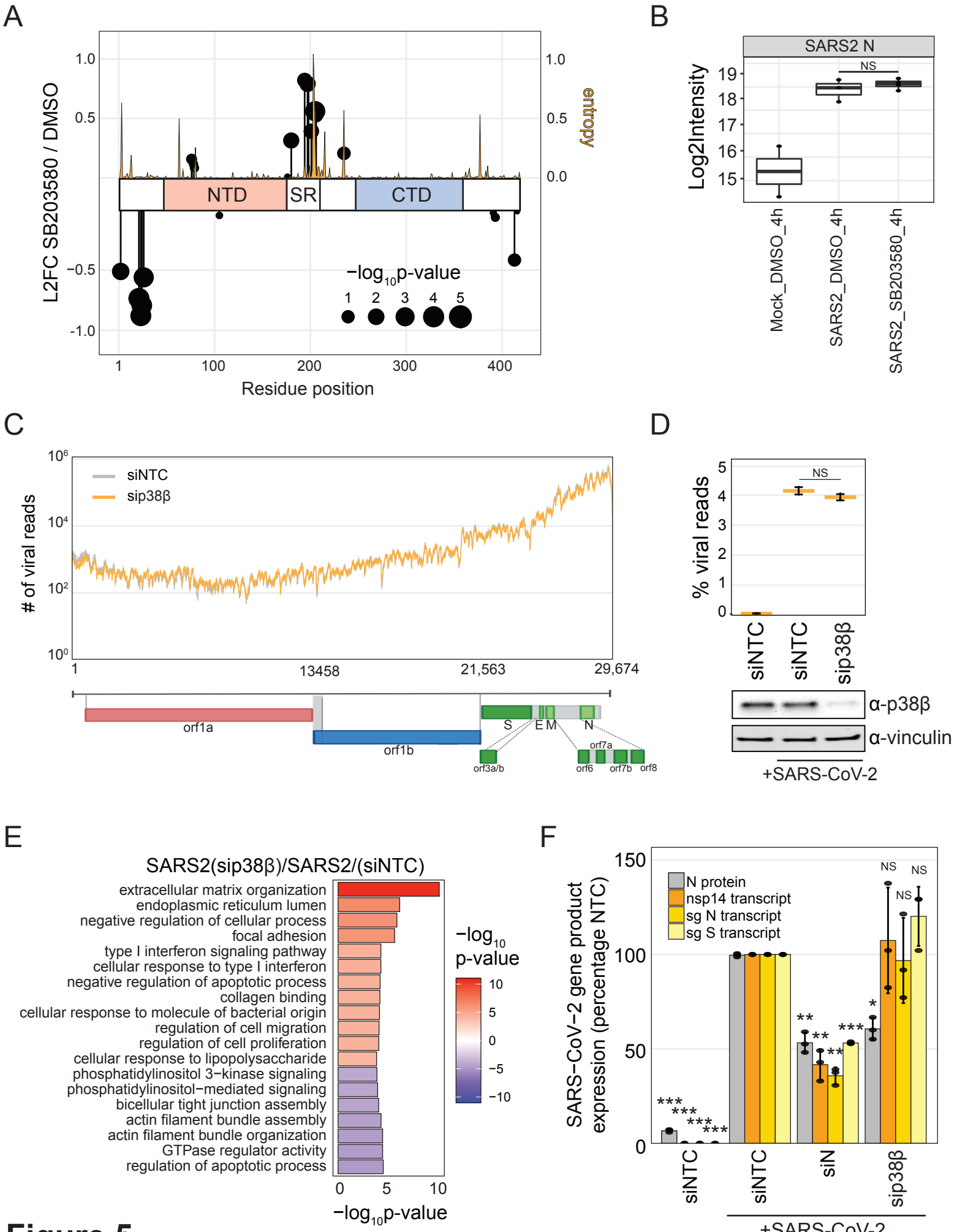
A
L2FC SB203580 / DMSO
entropy
NTD
SR
CTD
−log10p-value
1 2 3 4 5
Residue position
B
SARS2 N
Log2Intensity
NS
Mock_DMSO_4h
SARS2_DMSO_4h
SARS2_SB203580_4h
C
# of viral reads
siNTC
sip38β
13458
21,563
29,674
orf1a
orf1b
S
E M
N
orf3a/b
orf6
orf7a
orf7b
orf8
D
% viral reads
NS
siNTC
siNTC
sip38β
α-p38β
α-vinculin
+SARS-CoV-2
E
SARS2(sip38β)/SARS2/(siNTC)
extracellular matrix organization
endoplasmic reticulum lumen
negative regulation of cellular process
focal adhesion
type I interferon signaling pathway
cellular response to type I interferon
negative regulation of apoptotic process
collagen binding
cellular response to molecule of bacterial origin
regulation of cell migration
regulation of cell proliferation
cellular response to lipopolysaccharide
phosphatidylinositol 3−kinase signaling
phosphatidylinositol−mediated signaling
bicellular tight junction assembly
actin filament bundle assembly
actin filament bundle organization
GTPase regulator activity
regulation of apoptotic process
−log10 p-value
F
SARS−CoV−2 gene product expression (percentage NTC)
N protein
nsp14 transcript
sg N transcript
sg S transcript
siNTC
siNTC
siN
sip38β
+SARS-CoV-2

Figure 5

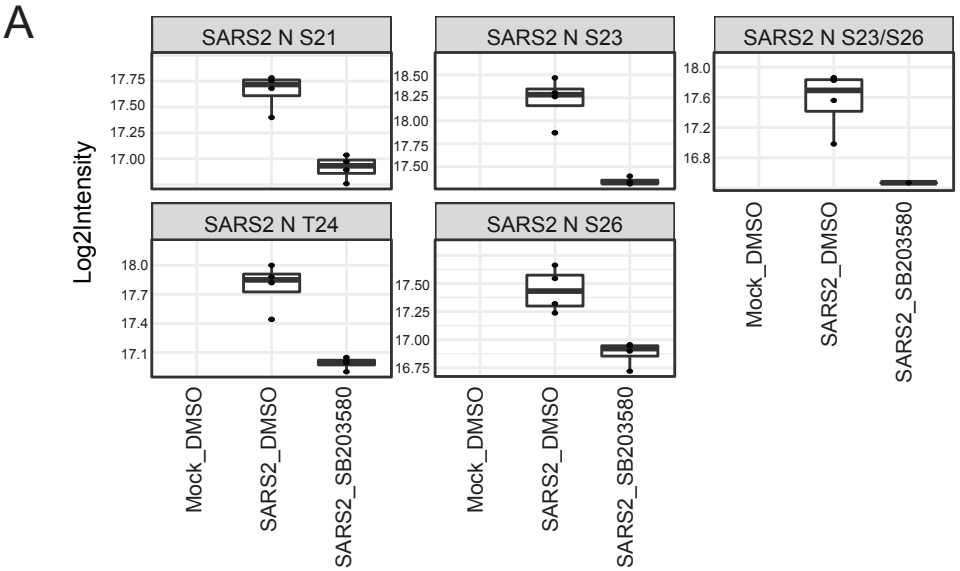

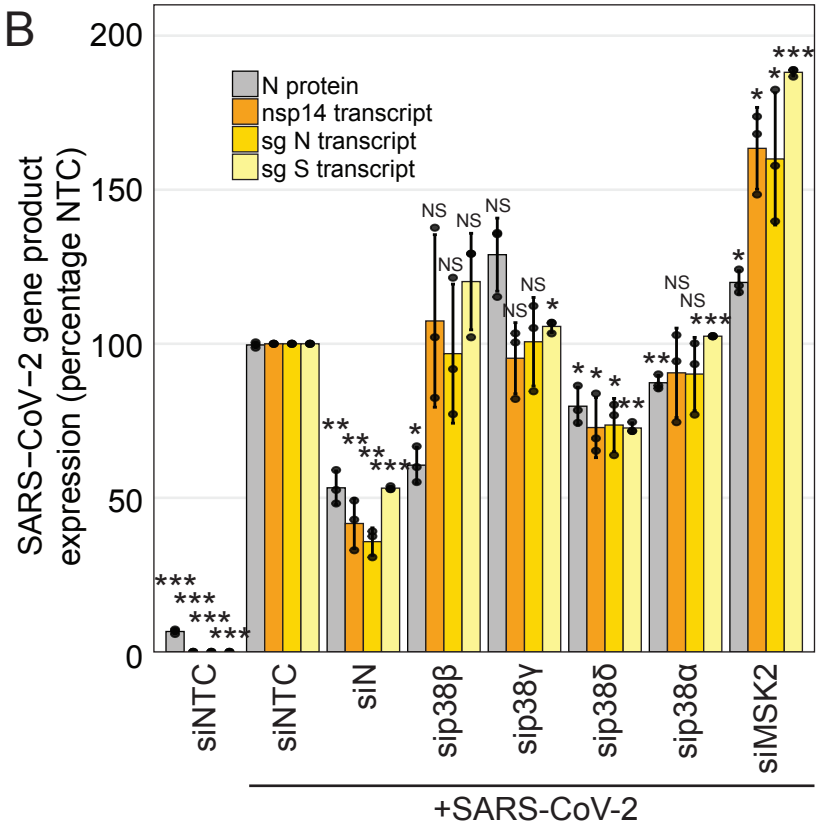

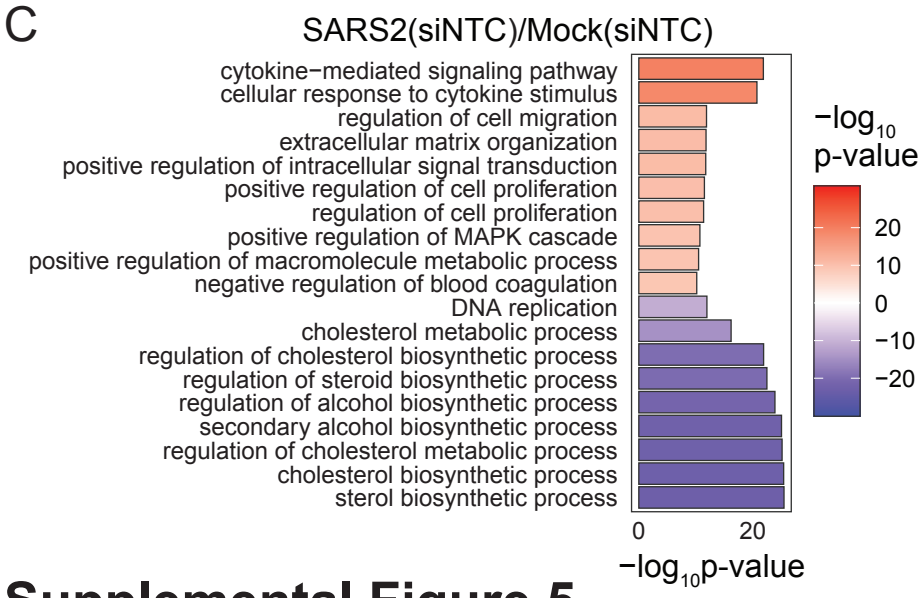

Supplemental Figure 5